Whisper-Gallery Microcavities Nano-sensing System Packaging

by

Wen Zhou
B.Eng., Beijing Institute of Technology, 2013

A Report Submitted in Partial Fulfillment of the
Requirements for the Degree of

MASTER OF ENGINEERING

in the Department of Electrical and Computer Engineering

Whisper-Gallery Microcavities Nano-sensing System Packaging

by

Wen Zhou
B.Eng., Beijing Institute of Technology, 2013

Supervisory Committee

Dr. Tao Lu, Supervisor
(Department of Electrical and Computer Engineering)

Dr. T. Aaron Gulliver, Committe Member
(Department of Electrical and Computer Engineering)

Supervisory Committee

Dr. Tao Lu, Supervisor
(Department of Electrical and Computer Engineering)

Dr. T. Aaron Gulliver, Committe Member
(Department of Electrical and Computer Engineering)

ABSTRACT

Whispering-gallery microcavities have been widely applied to many areas including sensing and nano-detection. To commercialize WGM sensors, packaging is necessary. This report introduces a design of a WGM nano-sensing system which has a compact volume and affordable price, making it suitable for practical use. It has a laser with a 980-nm central wavelength, an adjustable output power up to 160 mW, temperature control from 0 to 50 degrees, and a response power maximum of 10 mW. An associated display program was designed in LABVIEW to allow for the data to be captured from the device and sent directly to a PC or laptop through an AD converter included in the system. The progress of system design, module selection and assembly, calibration, program design of the device, and an application example of testing the Q factor of a microcavity are respectively discussed. The challenges, its possible solution, and future developments are also outlined at the end of this report.

Contents

List of Tables

List of Figures

ACKNOWLEDGEMENTS

I would like to show my gratitude to my advisor, Pr. Tao Lu, who has given me invaluable advice and constant help during this project as well as my postgraduate study. Also, I'd like to thank Wenyan Yu, Yu Hu, Xuan Du, Serge Vincent, Liao Zhang and other people who give me many suggestions.

DEDICATION

To my family

Chapter 1

Introduction

The whispering-gallery wave is a wave that propagates on a concave surface with low loss. [1] It was first introduced for sound propagating on the surface of the cylindrical wall in the St. Pauls Cathedral, London. [2] The whispering-gallery mode is partially confined by the optical field, because of the wave suppression due to a reflection effect of its curved edge, which is defined in a specific structure. Nowadays, there are many different types of WGM optical resonators including spherical, cylindrical, toroidal, ring and other forms. For instance, microcavities made of highly transparent dielectric media are optical resonators with very promising properties [3]. The photons travel around the whole microcavity along the inner surface. Resonance will occur when the photon round trip time exactly equals a multiple integer of the period of the photon oscillation. In that case, the microcavities work as a photon resonator that confines the photons in a tiny area located near the edge for a period of time longer than 1 microsecond [4, 5]. When a nano-particle adsorbs to the cavity surface, the path photons travel will be shifted by a small amount. This leads to a shift of the cavity resonance wavelength which can be detected for nano-sensing [6,7]. Due to the rapid development of modern WGM technology, the application of WGM has been reported in many research achievements but with limited exposure in the commercial domain. This is due to the challenges of efficient and robust coupling to WGM for practical applications. Besides, the fragility of the couplers in the practical application is another problem need to be solved. Recently, WGM resonator-based devices have become commercially available [8–11] because of a well-developed waveguide coupling technique. At the same time, the WGM ancillary equipment in the laboratory is still large, bulky and expensive. The total cost of the experimental facilities in the laboratory is more than 50 thousand dollars.

In this report, an integrated portable WGM nano-sensing system is introduced. The WGM ancillary equipment is integrated into a box-size device to keep the fiber tapered and protected and its modules are selected to make the device compact and affordable for movable and commercial usage. The cost of the device is less than one tenth of the traditional devices. When associated with a WGM resonator, this system can be considered as a nano-sensor system, which can be used outside the laboratory.

1.1 Report Outline

This report is structured as follows:

Chapter 2 introduces basic theory and principles of whispering-gallery mode resonators. The applications of the gallery mode resonators is mentioned in the later section.

Chapter 3 lists components for the package. The major functions and capabilities of each component are illustrated in this chapter.

Chapter 4 shows the system design. The related software used in the system is also described in this chapter.

Chapter 5 demonstrates details of the calibration and performance and stability tests, followed by an introduction of the data capture and display program associated with the system. An application of testing the Q factor is also discussed.

Chapter 6 discusses the advantages and disadvantages of this system. A prospect of the next generation product is depicted at the end of the chapter.

Chapter 2

Background

The whispering-gallery wave was first found by Lord Rayleigh in the 19^{th} century and named by the whispering-gallery of St. Paul's Cathedral in London. [2] It describes the phenomenon that sound uttered at one end of the dome could still be heard clearly at the other end. Figure 2.1 (a), 2.1 (b), 2.1 (c) show the figure of the dome of St. Paul's Cathedral, the sketch of the whispering gallery, and the sound paths in a circular whispering gallery, respectively. In free space, the loss of the intensity of the sound is proportional to the square of the distance the sound travels. However, in the cylindrical walls the loss is much smaller, which decreases only proportional to the travel distance. Therefore, the sound could still be heard clearly over a long distance.

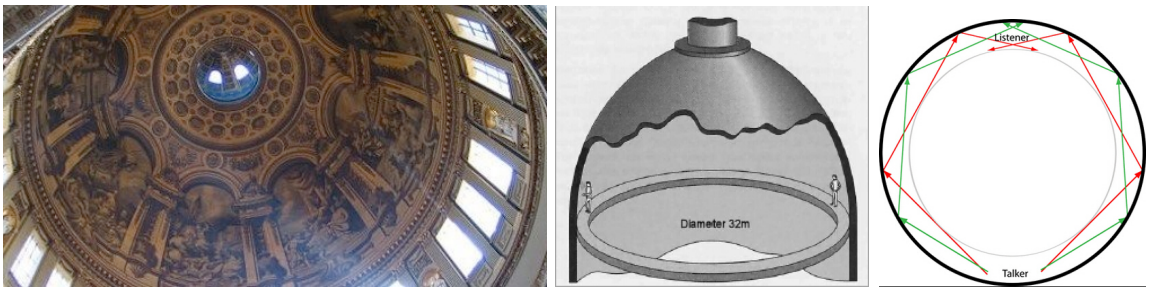

(a) (b) (c)

Figure 2.1: (a)A look at the dome of St. Paul's Cathedral from below[1] (b) A sketch of the whispering gallery[2] (c)Sound paths in a circular whispering gallery[3]

[1]http://strangesounds.org/wp-content/uploads/2013/11/whisperinggallery1.jpg
[2]http://www.chm.bris.ac.uk/ chjpr/characterisation2.html
[3]http://www.sonicwonders.org/images/whispering%20gallery.gif

At the beginning of 20^{th} century, researchers demonstrated that the electromagnetic waves have almost the same phenomenon with the whispering-gallery waves in dielectric spheres. Decades passed by, the application of whispering-gallery mode in optics began to be widely developed. [12] Nowadays, modern dielectric optical resonators based on whispering gallery theory gain its popularity becomes much more sensitive because of its high Q factor, low mode volumes, on-chip size and ease of fabrication.

2.1 Fundamental principle of WGM

To describe the field in the microsphere, we can use Maxwell equations, which consists of the Lorentz force law, forms of the foundation of classical electrodynamics, classical optics, and electric circuits:

$$\nabla \cdot \vec{D} = 0 \tag{2.1}$$

$$\nabla \times \vec{E} = \frac{-\partial \vec{B}}{\partial t} \tag{2.2}$$

$$\nabla \cdot \vec{B} = 0 \tag{2.3}$$

$$\nabla \times \vec{H} = \frac{-\partial \vec{D}}{\partial t} \tag{2.4}$$

$\vec{D}$ represents the electric displacement field, $\vec{E}$ describes the electric field, $\vec{B}$ indicates the magnetic field, and $\vec{H}$ is the magnetizing field. From equation (2.2), we could deduce the equation (2.5) by adding the curl operator to each side:

$$\nabla \times \nabla \times \vec{E} = -\nabla \times \frac{\partial \vec{B}}{\partial t} \tag{2.5}$$

As we already know, $\vec{B} = \mu \vec{H}$. Using this relationship in equation (2.5), we could get the deformation equation (2.6)

$$\nabla \times \nabla \times \vec{E} = -\mu \frac{\partial \nabla \times \vec{H}}{\partial t} \tag{2.6}$$

According to equation (2.4) and $\vec{D} = \epsilon\vec{E}$, we could transfer equation (2.6) to equation (2.7):

$$\nabla \times \nabla \times \vec{E} = -\mu\epsilon\frac{\partial^2 \times \vec{E}}{\partial t^2} \tag{2.7}$$

In mathematics and physics, the vector Laplace operator, denoted by ∇^2, named after Pierre-Simon Laplace, is a differential operator defined over a vector field. From the properties of the vector Laplacian of a vector field $\vec{A}$, we have:

$$\nabla^2\vec{A} = \nabla(\nabla \cdot \vec{A}) - \nabla \times (\nabla \times \vec{A}). \tag{2.8}$$

From the equation (2.8), we find the second term of the right part of the equation is same as the left term of the equation (2.7) for a vector. In our case, the vector Laplacian of the electric field could be expressed as:

$$\nabla^2\vec{E} = \nabla(\nabla \cdot \vec{E}) - \nabla \times (\nabla \times \vec{E}). \tag{2.9}$$

The first term in the equation (2.9) on the right side of the equal sign could be expanded using $\vec{D} = \epsilon\vec{E}$:

$$\nabla(\nabla \cdot \vec{E}) = \frac{1}{\epsilon}\nabla(\nabla \cdot \vec{D}) \tag{2.10}$$

From the very beginning, we have the Lorentz force law of the Maxwell equation, $\nabla \cdot \vec{D} = 0$. Therefore the equation (2.10) obviously equals to 0:

$$\nabla(\nabla \cdot \vec{E}) = \frac{1}{\epsilon}\nabla(\nabla \cdot \vec{D}) = 0 \tag{2.11}$$

Then the equation (2.9) could be simplified as follows:

$$\nabla^2\vec{E} = -\nabla \times (\nabla \times \vec{E}) = \mu\epsilon\frac{\partial^2 \times \vec{E}}{\partial t^2} \tag{2.12}$$

$\vec{E}$ is a function of time and space. It can be solved by separation of variables. By assuming the field is monochromatic and the dielectric constants are independent of time, we obtain:

$$[\nabla^2 + n^2(\vec{r})k_0^2]\vec{E}(\vec{r}) = \vec{0} \tag{2.13}$$

Equation(2.13) is called Helmholtz equation. $k_0 = \frac{\omega}{c}$ is the vaccum wave number,$n(\vec{r})$ is the complex refractive index.

In a cylindrical coordinate system, the Helmholtz equation can be expressed as:

$$[\frac{\partial^2}{\partial\rho^2}+\frac{1}{\rho}\frac{1}{\partial\rho}+\frac{1}{\rho^2}\frac{\partial^2}{\partial\phi^2}+\frac{\partial^2}{\partial z^2}+n^2(\vec{r})k_0^2]\vec{E}(\rho,z,\phi)=\vec{0} \tag{2.14}$$

By using numerical techniques such as finite element method (FEM), we can solve the equation to simulate the propagation of the WGM. [13]

2.2 Application of whispering-gallery mode resonators

To date, the major WGM devices applied in practice could be sorted into two kinds: passive devices and active devices.

2.2.1 Passive WGM device

The most important property of the spectrum of WGM is its narrow linewidth. This makes whispering-gallery resonators useful for many practical applies. This section will introduce some applications, especially in filter and sensor. One of the WGM devices is photonics filter [14, 15]. The traditional microwave filters have narrow bandwidth and wide tunability, which are ideal for the realization of modern communications and radar usage. The narrow bandwidth means the large capacity of the channels in communications band, and the tunability naturally allows spectral diversity and high efficiency. However, microwave filters have a flat passband and the narrow bandwidth and wide tunability cannot be reached at the same time due to the high side-mode rejection.

Photonics filters based on WGM give a new way to overcome these problems as shown in the follows.

a. Single resonator filters

The transmission coefficient of a monochromatic electromagnetic wave in a single prism configuration could be expressed as follows

$$t=\frac{\gamma_c-\gamma-i(f-f_0)}{\gamma_c+\gamma+i(f-f_0)} \tag{2.15}$$

where t represents the amplitude transmission, f is the frequency and γ, γ_c and f_0 represent the absorption, coupling linewidth, and resonance frequency of a mode in a resonator, respectively (the $|f-f_0|$ is assumed much less than the cavity free spectral

range). The power transmission $|t|^2$ in the resonator is a Lorentzian. The condition $\gamma = \gamma_c$ is related to critical coupling of the resonator [163,164].

It should be noted that in a single coupling prism, the filter is characterized by absorption resonance while in the two-prism set the value is represented by transmission resonance. In the latter case, the amplitude transmission and reflection coefficients in the resonator could be represented as

$$\left.\begin{array}{l} t = \frac{\gamma_c}{\gamma_c + i(f - f_0)} \\ r = \frac{i(f - f_0)}{\gamma_c + i(f - f_0)} \end{array}\right\} \tag{2.16}$$

where t and r represent the amplitude transmission and reflection, respectively. We assume $\gamma_c \gg \gamma$ for simplicity.

There are a ring-shaped WGRs based filters studied in previous research [16, 17]. The single-ring resonators based filter is integrated with semiconductor optical amplifiers based on GaInAsP-InP in some researches [18]. A sloped refractive index square or rectangular area coupled with two dielectric waveguides can be considered as an integrated optical resonator. Its applications including filtering are developed recently [19].

But unfortunately, the Lorentzian line shape filter function integrated with a single microresonator has a limited ability in practical applications due to many systems requiring large side-mode rejection, a narrow passband and wide tuning range at the same time.

b. Tunable filters

During the transportation of high Q's optical spectra, the WGM filter made on silica ring resonators has limited abilities in their microwave Q and convenient tuning technique. The applied strain [20,21] and temperature [22] have been previously used in mechanical trimming of WGMs. The tuning range of the mechanical is as wide as tens of nanometers, but these methods are not suitable for many applications due to its low speed and inaccuracy. For a high Q resonator, especially with a narrow filter bandwidth, the tuning accuracy is extremely important. Nowadays, an all-optical tunable filter based on discontinuity-assisted ring resonators without the shortcomings mentioned above proved in theory. [23] A demonstration has showed a new technique for WGM resonance tuning, which uses a microring structure and a photosensitive coating. Microrings made of glass were dipped in a polymer coating material and were exposed to ultraviolet (UV) light in that case. Because of the polymer-induced

absorption, this method could only produce resonators with relatively low Q (about 800), but it still has large tunability of the optical resonance of the microring, which means it could be applied in wavelength selecting uses. [24] Recently, A method based on photobleaching chromophores has been proposed for trimming the wavelength of polymer optical microresonator-based optical notch filters. [25] A maximum shift of $-8.73nm$ in wavelength was demonstrated in that case. This resonator has an intrinsic Q value between $\sim 2 \times 10^4$ and a finesse of ~ 10 at the same time.

By exploiting the photosensitivity of the germanate silica glass, we could also realize trimming the frequency of microresonators. When exposed to UV light, this material could alter its index of reflection by undergoing a small permanent change in structure. A uniform change in the resonant frequency happens due to the spatially uniform translation in the index of refraction in the WGRs. This kind of tunable resonator, as well as a second-order optical filter made by two coupled resonators, which consist of one tunable resonator, was practically realized for optical high Q (10^8) WGMs. [26, 27] Nowadays, a high Q microwave filter with a 10 MHz linewidth and a tuning range larger than 10 GHz [28], which fabricated optical WGM resonators with lithium niobate [29] is reported. The $LiNbO_3$ single resonator could reach its best tunability, which is around $\pm$20 GHz by adding a $\pm$50 V DC voltage to an electrode over the resonator.

c. High-order filters

The coupling fiber resonator is widely used as an optical filter [30, 31], because of its small size, low loss and integrability into optical networks. On the basis of a multi-polar and manufacturing silicone cascade, the WGRs high-Q filter has proved it could provide compacting package and strong performance, typically between 10 to 100 GHz bandwidth and the corresponding Q dimming sequence $10^5 - 10^4$. [32,33] And they actually are commercially available. Their passband provides a flat top and sharp skirt for high-performance applications. Since the microwave signal photon system is an optical carrier sideband, these filters could be used at any microwave frequency, thereby providing the same characteristics as a whole band, from 10-100 GHz and higher. High-Q WGM resonators can be applied to build microwave photons filters with high orders of magnitude narrow bandwidth. A second-order first narrowband optical filter, which is made of a high-Q WGM resonator and a tunable WGM resonator has already been achieved [27].

2.2.2 Active WGM device

The nonlinear optical process is enhanced by the small mode volumes and high-Q factors of WGMs. This enhancement gives the WGR-based nonlinear optic devices unique characteristics. For instance, the usage of WGM makes the lasing and wave-mixing possessing microwatt thresholds. The laser's narrow linewidth of WGMs provides narrow spectral characteristics.

a. Continuous-wave WGM lasers

Laser is the one of the most used applications of WGRs. The high quality factor of the resonators provides a significant reduction of the lasing threshold. The earliest WGM lasers were produced by the solid materials. [34, 35] The next development step on the WGM-based lasers happened in liquid aerosols and the individual liquid droplets area. [36] Recently, ultranarrow-linewidth and ultralow-threshold lasers based on WGM resonators have been reported in researches. [37, 38]

b. Resonator-modified scattering

The three most famous scattering processes playing significant roles in WGRs are Brillouin, Raileigh, and Raman scattering. The Stimulated Brillouin scattering (SBS) was first demonstrated in liquid droplets. [39,40] The Rayleigh scattering based interfacing WGM resonator is reported recently. [41] And the Raman scattering based CW lasers is attractive for sensing, spectroscopy because of it enhances the optical power in substantial with large tunability and low threshold.

c. Switches and modulators

WGM resonators can be used as compact and efficient optical switches and modulators. The studies of optical switches based on WGM are still theoretical. However, a possibility of creating a quantum-mechanical computer based on the nonlinear optical switches is already reported [42] and discussed in these decades.

Chapter 3

Components of a WGM Nano-sensing System

A typical whisper-gallery sensing system consists of a source laser which has a stable and unique wavelength, a whisper-gallery micro cavity resonator matching the laser wavelength, a laser diode sensitive in the related wavelength and an analog-to-digital device. Fig 3.1 shows a typical WGM sensing system used in biosensing.

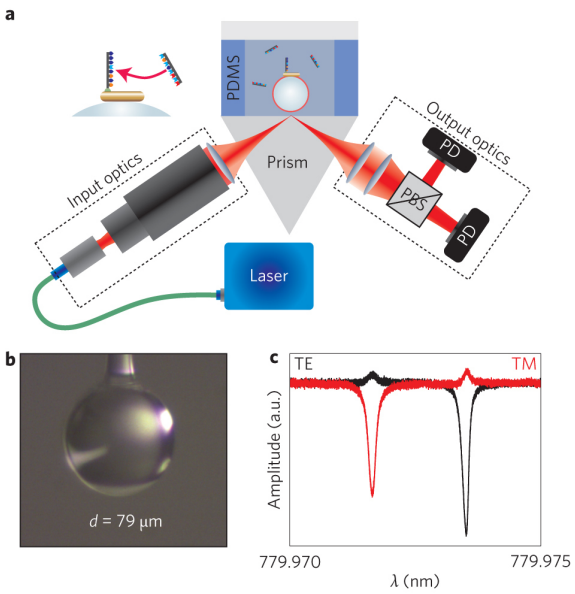

Figure 3.1: A typical WGM sensing system used in biosensing[1]

[1]http://www.nature.com/nnano/journal/v9/n11/images/nnano.2014.180-f1.jpg

3.1 Laser production module

3.1.1 Laser diode module

A laser diode is a semiconductor laser pumped in the active medium which is formed by a p-n junction of a semiconductor diode. One of the most common lasers is the Fabry-Perot laser. It is basically an LED associated with a pair of end mirrors. The mirrors are needed to provide the appropriate conditions for lasing to occur. The Fabry-Perot laser is named from the fact that its cavity plays a role as a Fabry-Perot resonator. By explaining the principle of the Fabry-Perot filter, we could have a better understanding of the operation principle of the Fabry-Perot laser. Figure 3.2 illustrated the principle of the Fabry-Perot filter.

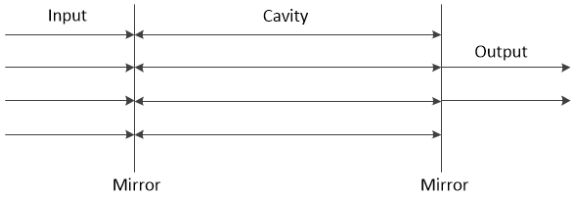

Figure 3.2: A sketch of Fabry-Perot filter. The cavity of the Fabry-Perot filter is a pair of partially mirrors. The light enters the cavity through one mirror and leaves through another. Only the wavelengths resonated with the cavity can pass through the mirror.

When you fix two mirrors opposite to each other, they become a resonant cavity. Light will bounce between the two mirrors. When the optical path length between the two mirrors equals integral multiples of half wavelengths, the light will reinforce itself and the other lights whose wavelengths that are not resonant are reflected away. The optical path length is the product of the geometric distance that light travels and the refractive index of the medium it propagates. The wavelengths produced from the Fabry-Perot cavity are related to the distance between the mirrors by the following formula (ignoring the frequency pulling effects [43]):

$$C_l = \frac{\lambda x}{2n} \tag{3.1}$$

where λ represents the laser wavelength, C_l indicates the length of the cavity, x is an arbitrary integer and n is the refractive index of active medium. The laser module used in our system is ADC Telecommunications 980nm laser module model

980S160GBAFC which is shown in Figure 3.3. It is a single-frequency laser diode that has a maximum output power of 160 mW of 980nm central wavelength. The ADC Telecommunications 980nm is well-suited for low-noise pumping applications. It comes with the internal TEC optional function which is compatible with the ILX laser controller ldc-3722b and laser diode mount ldm-4984. Table 3.1 shows the specifications for the ADC Telecommunications 980S160GBAFC.

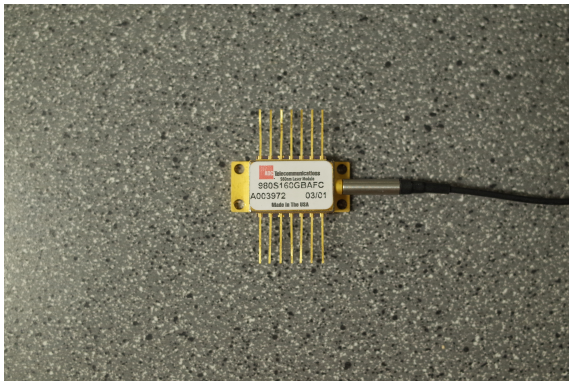

Figure 3.3: ADC Telecommunications laser module model 980S160GBAFC

ADC Telecommunications 980S160GBAFC	
LD Reverse Voltage (Max)	2.5 V
Absolute Max Current	200 mA
Absolute Max Power	160 mW
PD Reverse Voltage (Max)	2 V
Operating Temperature	0 to 50 °C
Storage Temperature	-10 to 65 °C

Table 3.1: Specifications for ADC 980S160GBAFC[2]

Figure 3.4 shows the drawings and pin identifications of a typical 14-pin butterfly laser module including the ADC 980S160GBAFC.

3.1.2 Laser controller

The laser controller is used to produce a stable and accurate driver current to guarantee the reliability and stability of the laser output. The laser diode controller used

[2]https://www.thorlabs.com/thorcat/QTN/DBR976S-SpecSheet.pdf

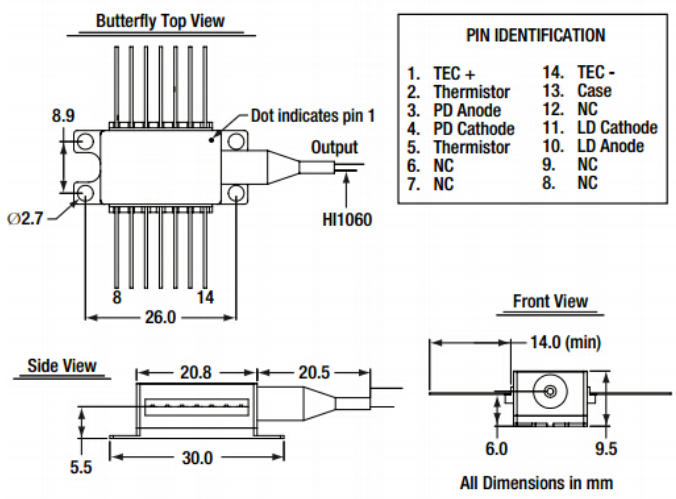

Figure 3.4: 14-pin butterfly laser module drawings and pin identifications[3]

in this project is ILX Lightwave ldc-3722b as shown in Fig 3.5. This laser diode controller is a combination current source and temperature controller. The current source offers a stable output with a full current limit and multiple laser protection features. Moreover, with the built-in temperature controller, the laser could provide precision laser temperature control for a wide range of temperatures.The specifications of the ldc-3722b laser current source are shown in Table 3.2, and the temperature controller specifications are shown in Table 3.3.

Figure 3.5: ILX Lightwave laser diode controller model 3722b[4]

[3]https://www.thorlabs.com/thorcat/QTN/DBR976S-SpecSheet.pdf

[4]http://oakbluffclassifieds.com/Ads-By-members/Ilx-ldc-3722B-laser-diode-controller-as-is-picture.jpg

Current Source	**200 mA range**	**500 mA range**
Set Point Accuracy	±100 μA	±250 μA
Set Point Resolution	4μA	10μA
Compliance Voltage (fixed)	6.5 V maximum	6.5 V maximum
Temperature Coefficient	< 50 ppm/°C	< 50 ppm/°C
Stability for 10 min	< 20ppm	< 20ppm
Stability for 24 hours	< 50ppm	< 50ppm
Noise and Ripple		
High Bandwidth Mode:	< 4 μA rms	< 4 μA rms
Low Bandwidth Mode:	< 2 μA rms	< 2 μA rms
CW Mode (with 320 cable):	< 0.8 μA rms	< 0.8 μA rms
Worst Case Transients		
Operational:	< 1 mA	< 1 mA
Power-line induced:	< 5 mA	< 5 mA
Photodiode Feedback Range	5 to 5000 μA	
Photodiode Feedback Output Stability	± 0.02%	
Photodiode Feedback Accuracy	± 2.5 μA	
Photodiode Feedback Bias Voltage	0 - 5 V reverse bias (±10%)	
Output Current Range	0.00 to 200.00 mA	0.00 to 500.00 mA
Output Current Resolution	0.01 mA	0.01 mA
Output Current Accuracy at 25 °C	±0.1mA	± 0.25 mA
Photodiode Current Range	0 - 5000 μA	0 - 5000 μA
Photodiode Current Resolution	1 μA	1 μA
Photodiode Current Accuracy	± 2.5 μA	± 2.5 μA
Responsivity Range	0 - 600.00 μA/mW	0 - 600.00 μA/mW
Responsivity Resolution	0.01 μA/mW	0.01 μA/mW
Optical Power Range	0 - 200.00 mW	0 - 200.00 mW
Output Power Resolution	10μW	10 μW
Current Limit Range	0 - 202 mA	0 - 505 mA
Current Limit Resolution	1 mA	2 mA
Current Limit Accuracy	± 2 mA	± 5 mA

Table 3.2: Specifications for ldc-3722b laser current source[5]

[5]http://www.artisantg.com/info/P_MBVvo.pdf

TEC Output		
Output Type	Bipolar constant current source	
Compliance Voltage	4 Volts at 4 Amps	
Maximum Current Output	4 Amps	
Maximum Output power	16 Watts typical	
Current Limit Control Range	0 - 4 A	
Current Limit Accuracy	± 50 mA	
Ripple/Noise	< 1 mA rms	
Temperature Range	−99°C to +150 °C	
Temperature	Resolution	Accuracy
−20°C/0°C/20°C/50°C	± 0.1°C	± 0.2°C
LM335 Setting Accuracy	±0.2°C	
AD590 Setting Accuracy	±0.2°C	
Short Term Stability	± 0.01°C or better, over 1hr.	
Long Term Stability	± 0.1°C or better, over 24hours.	
Sensor Type	2-wire thermistor	
Usable Thermistor Range	25 Ω to 450 kΩ typ.	
LM 335 Voltage	$V(25\ ^\circ\text{C}) = 2980$ mV; $V_T = 10$ mV/°K	
LM335 Bias	1 mA	
AD590 Current	$I(25\ ^\circ\text{C}) = 298.2\ \mu$A; $I_T = 1\ \mu$A/°K	
AD590 Bias	+8 VDC	
Thermistor Sensing Current	10 μA or 100 μA (user selectable)	
TEC Display		
Maximum Current Reading	4.000 Amps	
Maximum Temp Reading	199.9 °C	
Current Resolution	0.001 Amps	
Current Display Accuracy	± 0.02 Amps	
Temperature Resolution	0.1 °C	
Temperature Display Accuracy	±0.2 °C	
Thermistor Resistance Resolution	0.01 kΩ at 10 μA setting; 0.001 kΩ at 100 μA setting;	
Thermistor Resistance Display Accuracy	±0.05 kΩ at 10 μA setting; ±0.005 kΩ at 100 μA setting;	

Table 3.3: Specifications for ldc-3722b temperature controller[5]

3.1.3 Laser diode mount

The laser diode mount we use in this system is ILX Lightwave LDM-4984 which is shown in Figure 3.6. The laser diode mount 4984 is designed for a typical butterfly 14-pins laser diode packages. It comes with zero insertion force sockets and spring-loaded clamps that facilitate easy mounting. It supports the ILX standard 9-pin input with extra configurable pins for accommodating virtually any laser diode pin configuration. Figure 3.7 shows the bottom view of a typical LDM-4984. To remove the cover, we should hold the mount upside down, then unscrew four hexagonal screws. The laser sockets are connected to pin headers through the printed circuit board, the numbers next to the headers indicate the pin number of the laser. These two 9-pin connectors are the laser current control and laser internal temperature control, respectively. There is another 9-pin connector opposite to the two connectors designing for laser package temperature control option. Color-coded wires are soldered to the two sides of the 9-pin connectors and unterminated end. These connectors are mated with the ldc-3722b laser controller, which means the pin designations are pre-determined by the instrumentation, therefore, we could pair the ldc-3722 b and ldm-4984 directly.

Figure 3.6: ILX Lightwave laser diode mount model 4984[6]

By connecting the color-coded wires with the relative pin on the header, the mount for our laser diode is configured.

A typical set for a laser diode with an optional internal temperature control is given in the Table 3.4.

[6]https://assets.newport.com/webDocuments-EN/images/70022505_LDM-4980_IX.pdf

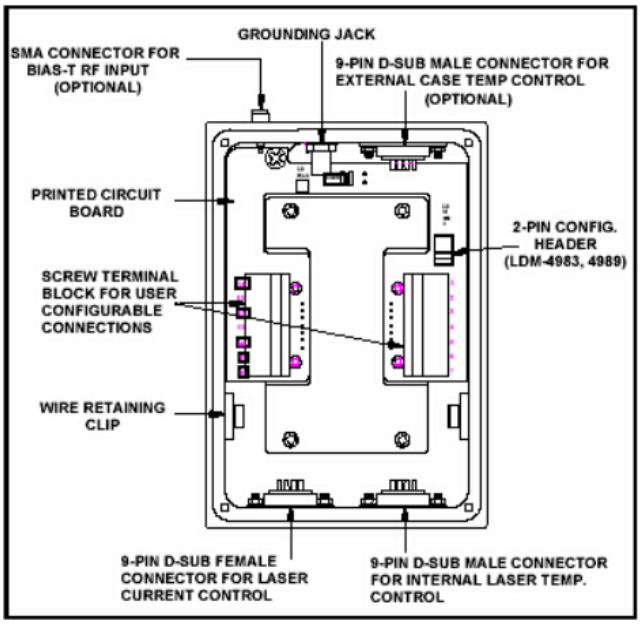

Figure 3.7: Bottom view of the ILX Lightwave laser diode mount model 4984(cover removed)[7]

Pin #	Description	Pin #	Description
1	Peltier Cooler (+)	8	Not Connected
2	Thermistor	9	Not Connected
3	Monitor Anode (−)	10	Laser Anode (+)
4	Monitor Cathode (+)	11	Laser Cathode (−)
5	Thermistor	12	Not Connected
6	Not Connected	13	Case Ground
7	Not Connected	14	Peltier Cooler (−)

Table 3.4: Laser Diode Pin Configuration with Internal TEC[8]

3.2 Laser receiver module

In our system, the laser receiver module could be simply separated into two parts. A photodiode sensitive to the laser frequency is the most important part, and we still need a power supply to guarantee the photodiode working accurately and stably.

[7]http://assets.newport.com/web900w-EN/images/32926.jpg
[8]http://assets.newport.com/webDocuments-EN/images/4980_Telecom_Laser_Diode_Mount.pdf

3.2.1 Photodiode module

The photodiode is a kind of semiconductor device that receives light and changes it into an electrical signal (current or voltage). When the photons are absorbed by the photodiode, the photocurrent is generated. There is still a small amount of current produced even in a dark environment, which is called the dark current. A typical photodiode consists of optical filters, compact lenses, and a laser receive surface. It usually has a longer response time when their surface area increases. The solar cell is a common and typical photodiode device.

The photodiode used in our system is Bookham Technology PP-10GC58J, which is shown in Figure 3.8. The specifications for the Bookham Technology PP-10GC58J were tested based on specifications of similar product. It is shown in Table 3.5.

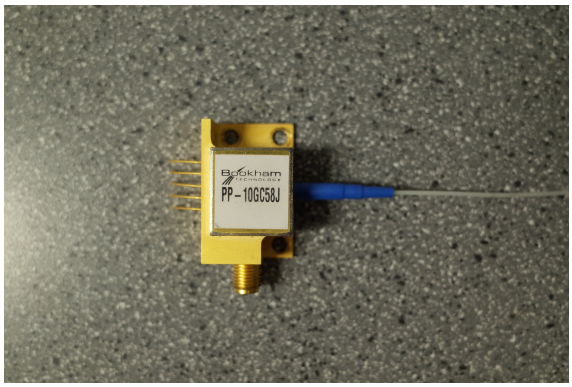

Figure 3.8: Bookham Technology PP-10GC58J photo-diode

Experimental performance of Bookham Technology PP-10GC58J	
Minimum output current	15.03 mA
Maximum output current	42.53 mA
Minimum response power	70.05 μW
Maximum response power	10.12 mW
response wavelength	980 nm
pin identifications	1 pin: 12 V DC, 3 pin: 7.7V DC, other pins: ground
Operating Temperature	0 - 50 °C

Table 3.5: Specifications for Bookham Technology PP-10GC58J

3.2.2 Power supply

To provide a 12 V DC power, we could use 8 AA batteries or use a 110 V AC - 12 V DC adapter. But an external 110 V AC - 12 V DC adapter could still have ripple fluctuation during its works. Therefore, an extra 12 V DC - 12V DC converter should be used in this method. The DC - DC converter is important in portable electronic devices, which may require different levels of DC power supplies. Considering the stability of the power source, we should use a 12 V DC - 12 V DC converter at the rear end of the 110 V AC to 12 V DC adapter instead of the batteries set, since the battery voltage declines as its energy drained. The 12V DC - 12V DC converter we use is CUI Inc PDS1-S12-S12-M-TR , shown in Figure 3.9(a). The Figure 3.9(b) shows a DC - DC converter suitable for 12V DC - 7.7V DC transferring.

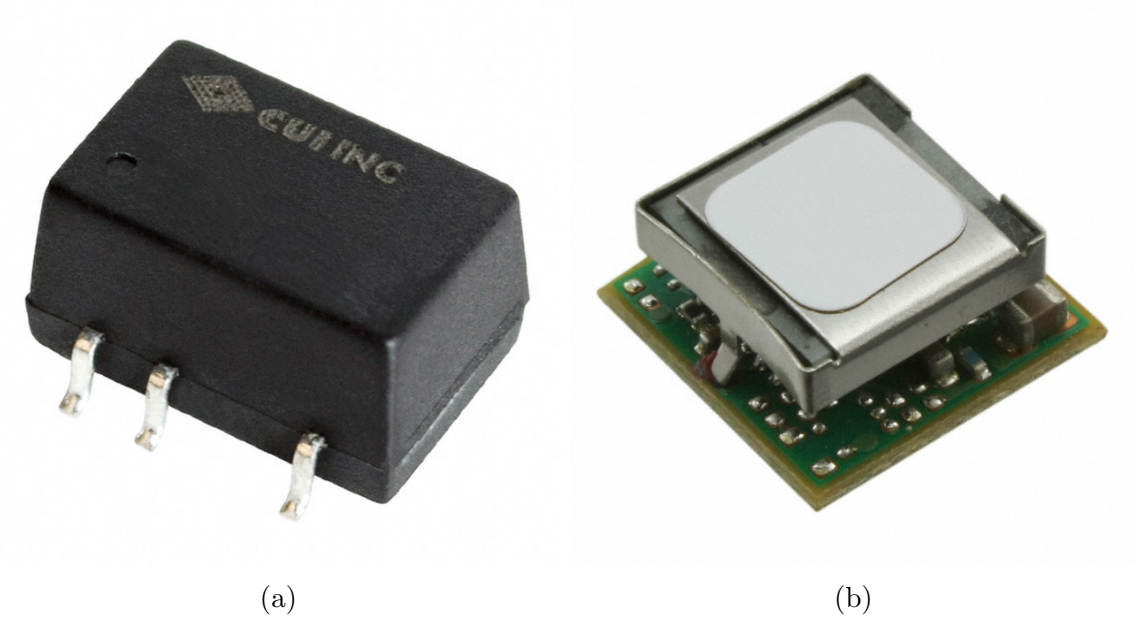

(a) (b)

Figure 3.9: (a)CUI Inc PDS1M series 12V DC - 12V DC converter[9] (b)GE Critical PicoTLynx 4A Power Modules[10]

The PDS1-M series DC - DC converter has a 1W isolated output with an efficiency up to 82% and a wide working temperature range (-40 to 105°C). It is mounted in a small package, and its specifications are shown in Table 3.6. The Figure 3.10 shows its mechanical drawing and pin identification.

To transfer from 12 Voltage DC to 7.7 Voltage DC, we could pick a DC-DC

[9]http://www.digikey.ca/product-detail/en/PDS1-S12-S12-M-TR/102-2680-1-ND/4009557
[10]http://www.digikey.ca/product-detail/en/APXK004A0X4-SRZ/555-1194-1-ND/2601276

converter whose input voltage range covers 12 V DC and output voltage range covers 7.7 V DC.

CUI Inc PDS1-S12-S12-M-TR	
Number of Outputs	1
Voltage - Input (Min)	10.8 V
Voltage - Input (Max)	13.2 V
Output Voltage	12 V
Current - Output (Max)	83 mA
Max Power (Watts)	1W
Package / Case	8-SMD Module (5 Leads)
Isolation Voltage	1.5kV (1500V)
Mounting Type	Surface Mount
Efficiency	81%
Operating Temperature	-40 to 105 °C

Table 3.6: Specifications for CUI Inc PDS1-S12-S12-M-TR[9]

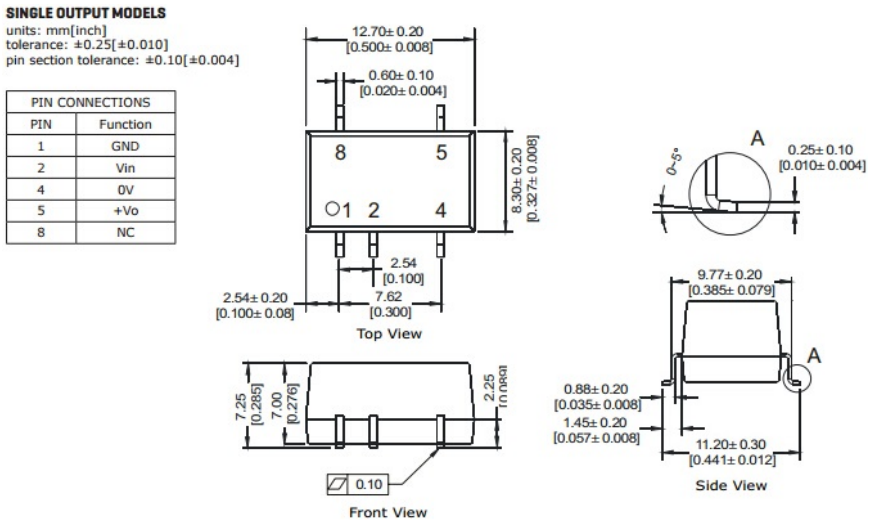

Figure 3.10: Mechanical drawing and pin identification for CUI Inc PDS1-S12-S12-M-TR[11]

The 16V PicoTLynx 4A Non-Isolated DC-DC Power Modules has a wide input range from 8 V to 16 V DC and it could provide a precisely regulated output voltage

[11]http://www.cui.com/product/resource/pds1-m.pdf

from 0.59V to 8.0 V DC, programmable via an external resistor. Its specifications are shown in Table 3.7.

Parameter	Device	Symbol	Min	Typ	Max	Unit
Operate Input Voltage	All	V_{IN}	8.0	–	16.0	V DC
Max Input Current	All	$I_{IN,max}$			6.5	A DC
Input No Load Current	$V_{O,min}$ $V_{O,max}$	$I_{IN,Noload}$ $I_{IN,Noload}$		18 96.1		mA mA
Input Standby Current	All	$I_{IN,standby}$		1.2		mA
Inrush Transient	All	I^2t		1		A^2s
Input Reflected Ripple Current	All			50		mAp-p
Input Ripple Rejection	All			-46		dB
Output Voltage Set point	All	$V_{O,set}$	-1.5		+1.5	% $V_{O,set}$
Output Voltage	All	$V_{O,set}$	-2.5		+2.5	% $V_{O,set}$
Adjustment Range	All	V_O	0.59		8.0	V DC
Output Ripple and Noise on nominal output						
Peak-to-Peak RMS	All All		- -	90 36	100 38	mV_{pk-pk} mV_{rms}
Output Current	All	I_O	0		4	A DC
Output Current Limit Inception	All	$I_{O,lim}$		200		% $I_{O,max}$
Output Short Circuit Current	All	$I_{O,s/c}$		200		% mA_{rms}
Switching Frequency	All	f_{sw}	-	600	-	kHz

Table 3.7: Specifications for 16V PicoTLynx 4A Non-Isolated DC-DC Power Modules[12]

Figure 3.11 shows the bottom view of the 16V PicoTLynx 4A Non-Isolated DC-DC Power Modules and Table 3.8 shows its pin identifications.

[12]http://www.digikey.ca/product-detail/en/APXK004A0X4-SRZ/555-1194-1-ND/2601276

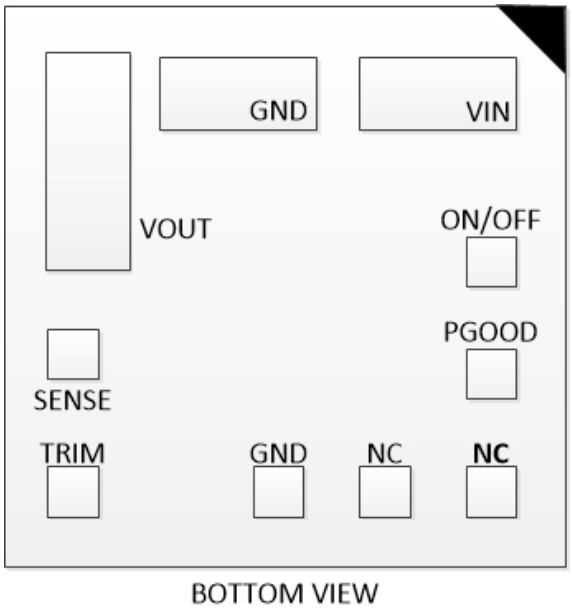

Figure 3.11: Bottom view of the 16V PicoTLynx 4A Non-Isolated DC-DC Power Modules

PIN	FUNCTION
1	ON/OFF
2	V_{in}
3	GND
4	V_{out}
5	SENSE
6	TRIM
7	GND
8	NC
9	NC
10	PGOOD

Table 3.8: Pin identifications for the 16V power module[12]

The features of the power modules include remote On/Off, over current and over-temperature protection, input under-voltage lockout and output voltage programming. By connecting a resistance to the T_{rim} and GND pins of the PCB, the output voltage can be set as any voltage between 0.59 V DC and 8.0V DC. There are certain restrictions on the output limit depending on the input voltage level. The relationship

between input and output voltage are shown in Figure 3.12.

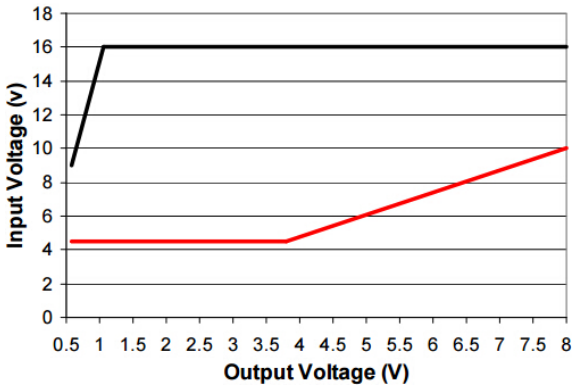

Figure 3.12: Output Voltage vs. Input Voltage Set Point Area[13]

When there is no external resistor between the trim and GND pins, the output voltage will be 0.59 V DC. To calculate the accurate output voltage, we could use the following equation:

$$R_{trim} = [\frac{5.91}{(V_0 - 0.591)}]k\Omega \tag{3.2}$$

The R_{trim} is the external resistor in $k\Omega$. And V_0 is the output voltage we want. Some common outputs are shown in Table 3.9.

$V_{O,set}$(V)	$R_{trim}(k\Omega)$
0.6	656.7
1.0	14.45
1.2	9.704
1.5	6.502
1.8	4.888
2.5	3.096
3.3	2.182
5.0	1.340
6.5	1.000
8.0	0.798

Table 3.9: R_{trim} values required for some common output voltages.

[13]http://www.digikey.ca/product-detail/en/APXK004A0X4-SRZ/555-1194-1-ND/2601276

After calculating, we can see if we need a 7.7 V DC output, the resistor R_{trim} should be around 830Ω.

To minimize the effects of distribution losses, we could regulate the voltage at the sense pin to use the remote sense feature. The difference between the output voltage pin and sense pin should be no larger than 0.5 V. When the remote sense feature is not used, we should connect the V_{out} pin to the sense pin as the Figure 3.13 shows.

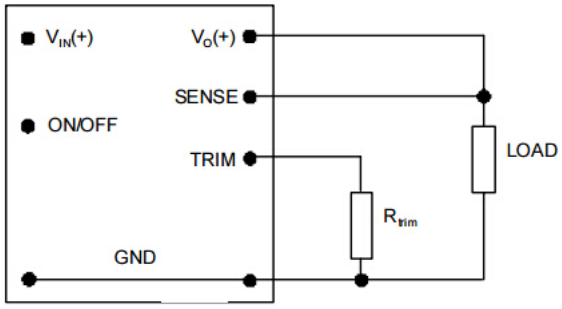

Figure 3.13: Configuration for selecting output voltage without remote sense.[14]

3.3 Analog-digital converter

The photodiode could transfer the light power in to a current signal, but we still need to transfer this analog current signal into a digital signal. An analog-to-digital converter (ADC) is a device that converts a continuous electric voltage to a digital number that represents the quantity's amplitude.

For convenience, we chose a USB port ADC device for transferring the signal to the PC after the ADC, which is National Instruments USB-6211 and shown in Figure 3.14.

The National Instruments USB-6211 is a bus-powered USB M Series multifunction data acquisition (DAQ) module optimized for superior accuracy at fast sampling rates, which is compatible with LabVIEW. It provides 16 analog inputs, 2 analog outputs, 4 digital inputs and 4 digital outputs with 250 kS/s single-channel sampling rate. The ranges of 4 inputs are programmable separated(±0.2 to ±10 V) and it comes with a built-in digital triggering and 2 counters. The specifications for the USB-6211 analog input and output are shown in Table 3.10 and Table 3.11.

[14]http://www.digikey.ca/product-detail/en/APXK004A0X4-SRZ/555-1194-1-ND/2601276

Analog Input	
Number of channels	8 differential or 16 single ended
ADC resolution	16 bits
DNL	No missing codes guaranteed
INL	Refer to the AI Absolute Accuracy Tables
Sampling rate	250 kS/s
Timing accuracy	50 ppm of sample rate
Timing resolution	50 ns
Input coupling	DC
Input range	±10 V, ±5 V, ±1 V, ±0.2 V
CMRR (DC to 60 Hz)	100 dB
Input impedance (device on)	
AI+ to AI GND	$> 10G\Omega$ in parallel with 100 pF
AI- to AI GND	$> 10G\Omega$ in parallel with 100 pF
Input impedance (device off)	
AI+ to AI GND	1200Ω
AI- to AI GND	1200Ω
Input bias current	±100 pA
Crosstalk (at 100 kHz)	
Adjacent channels	-75 dB
Non-adjacent channels	-90 dB
Small signal bandwidth (-3 dB)	450 kHz
Input FIFO size	4,095 samples
Scan list memory	4,095 samples
Data transfers	USB Signal Stream, programmed I/O
Overvoltage protection (AI < 0..31 >, AI SENSE)	
Device on	±30 V for up to two AI pins
Device off	±20 V for up to two AI pins
Input current during overvoltage condition	±20 mA max/AI pin

Table 3.10: Specifications for USB-6211 analog input[15]

[15]http://www.ni.com/datasheet/pdf/en/ds-9

Analog Output	
Number of channels	2
DAC resolution	16 bits
DNL	±1 LSB
Monotonicity	16 bit guaranteed
update rate	250 kS/s
Timing accuracy	50 ppm of sample rate
Timing resolution	50 ns
Output range	±10 V
Output coupling	DC
Output impedance	0.2Ω
Output current drive	±0.2 mA
Overdrive protection	±30 V
Overdrive current	2.4 mA
Power-on state	±20 mV
Power-on glitch	±1 V for 200 ms
Output FIFO size	8,191 samples shared among channels used
Data transfers	USB Signal Stream, programmed I/O

Table 3.11: Specifications for USB-6211 analog output[15]

To use the NI USB-6211, we should install the NI LabVIEW first, and then install the DAQmx library higher than Version 8.6 on PC. Then connect the USB port of USB-6211 to PC and its driver will be configured automatically. When the light on the USB-6211 turns green, the device is deployed successfully. Then connect 2 analog input Pins to the photo-diode module. The pinout figure of the USB-6211 is shown in Figure 3.15.

Figure 3.14: National Instrument USB-6211

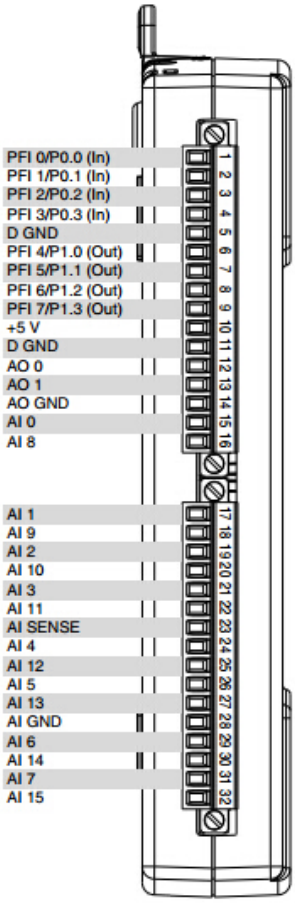

Figure 3.15: National Instrument USB-6211 pinout[16]

[16]http://www.ni.com/pdf/manuals/375195a.pdf

Chapter 4

Design and assembling

4.1 Nano-sensing system and device design

To build a sensing system, we should first consider the different signal types between modules mentioned above. The cables connecting the laser driver and the laser mount are typically 9-pin RS232 and its pinout is shown in Figure 4.1[1].

Figure 4.2 shows a schematic diagram of the system. The light green arrow in the diagram is the analog signal, the dark green arrow indicates the digital signal and the yellow arrow represents the optical signal. The optical signals are transmitted from the laser diode module to the sensing module and go back into the photodiode part of the system via optical fiber. To reduce losses, we should keep the fiber unbent or bending slightly and smoothly. And the ADC converts the analog signals from the photodiode into digital signals. The digital signals are finally received by the PC and demonstrated in LabVIEW.

Pin 1	DCD
Pin 2	RXD
Pin 3	TXD
Pin 4	DTR
Pin 5	GND
Pin 6	DSR
Pin 7	RTS
Pin 8	CTS
Pin 9	RI

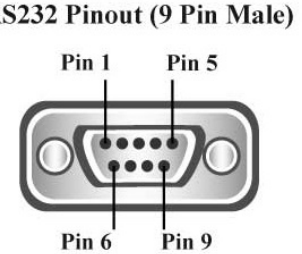

Figure 4.1: RS232 Pinout(9 pin male)[1]

[1]http://www.aw-el.com/win.htm

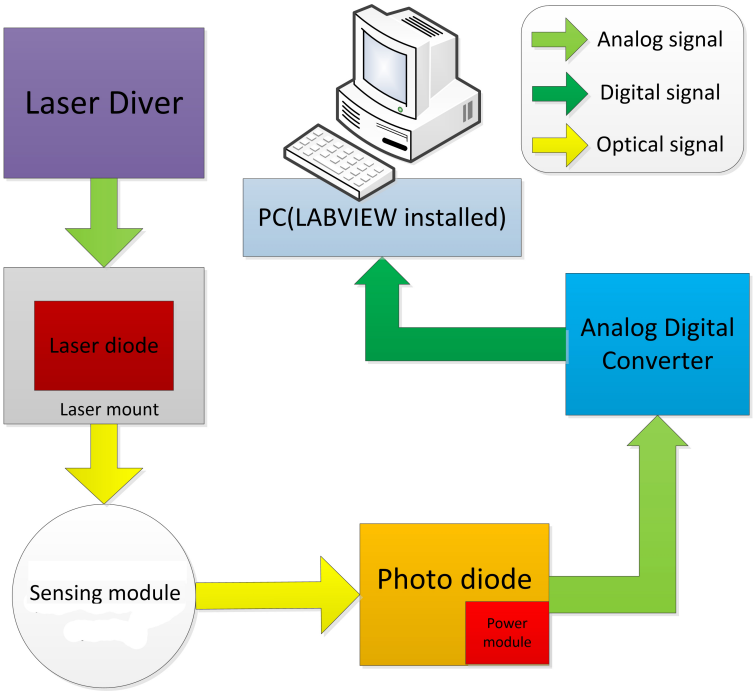

Figure 4.2: Schematic diagram of the sensing system

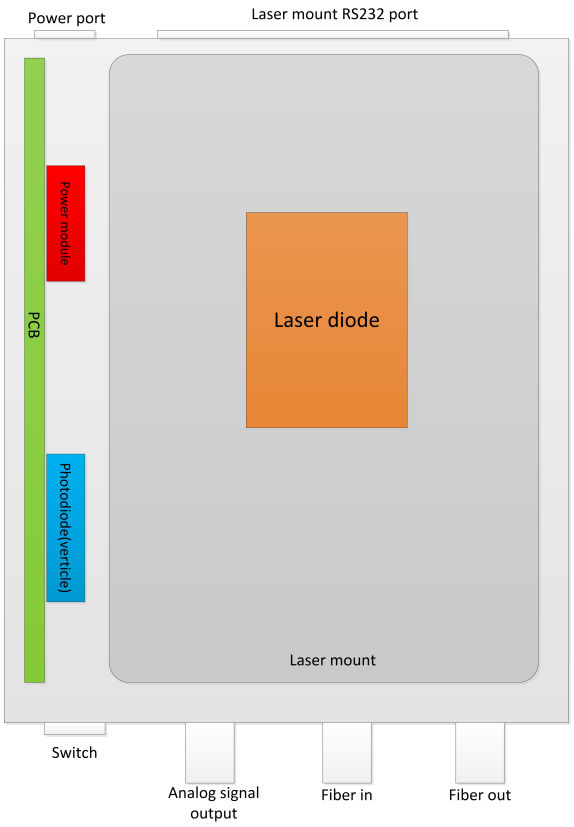

Figure 4.3: Drawing of the layout of the device box

In this project we only assemble and mount the laser diode module and photodiode module with the power module in an integrated box. A drawing of the optical and analog signal generation device is shown in Figure 4.3(cables are not shown in drawing). By integrating different modules together, the integrity, reliability and stability of the whole will be improved, which could be calibrated to test or detect different nano-sensing beads.

4.2 Assembling

The size top surface of the device box used in practical is 150 mm × 220 mm, and the size of the bottom surface is 145 mm × 215 mm, with a height of 60.5 mm. Figure 4.4 shows a design sketch of this box in SolidWorks. The 4 holes in the front view are designed for a switch, photodiode analog output, laser in, laser out respectively. The slots on the back are for the 9-pin RS232 connector of the laser driver and the power socket.

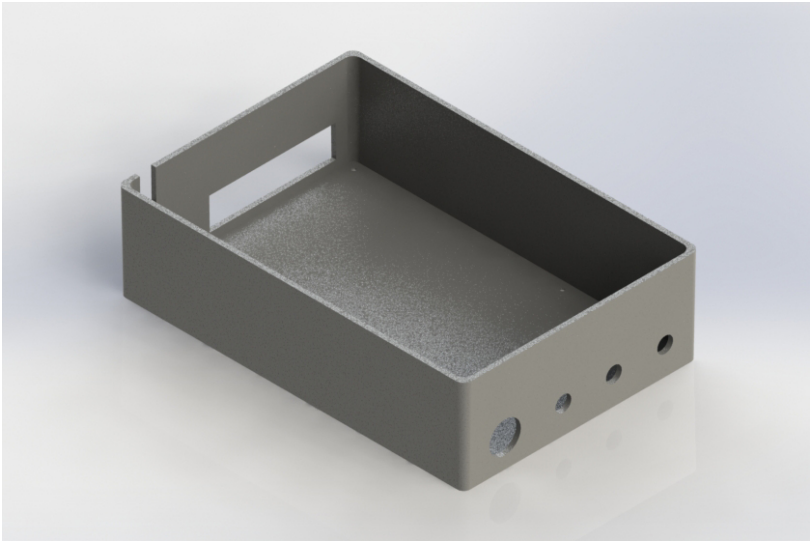

Figure 4.4: Design sketch of the device box

During the practical mounting process, we need to use an electric iron to integrate the power module onto the PCB. Figure 4.5 shows a PCB integrated with the photodiode and the relevant power supplies. An external 12V power should be used associated with the power socket. Moreover, the switch is connected with the power supplies through the other wires. A special aluminum stand is designed for the PCB to be placed vertically in the box.

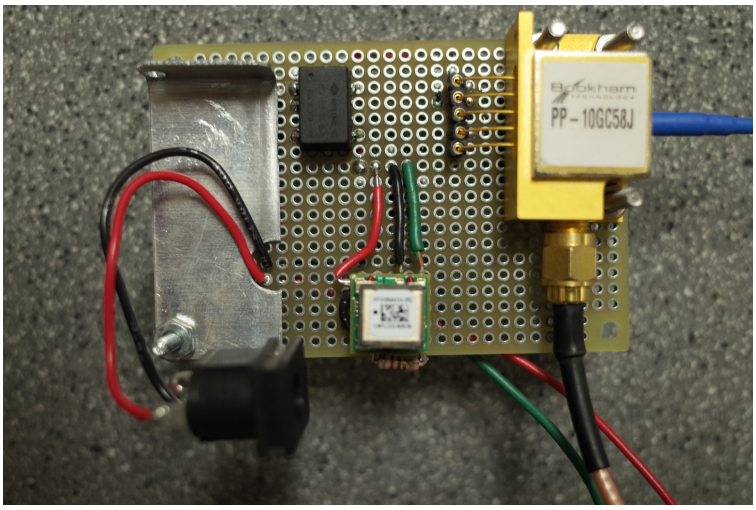

Figure 4.5: The PCB integrated with the photodiode and the relevant power supplies. A special aluminum stand is designed for the PCB standing vertically in the box.

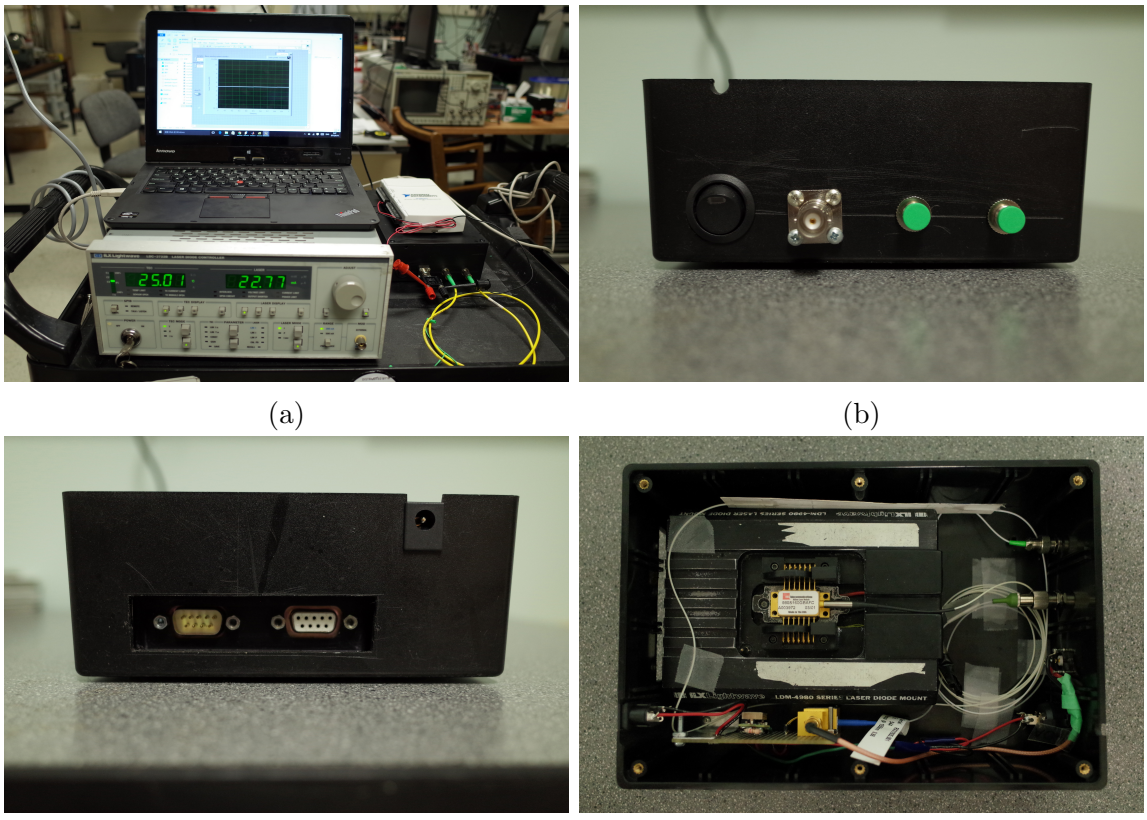

(a) (b)

(c) (d)

Figure 4.6: (a)The view of the entire system including the mounted device. (b)The front view of the mounted device. (c)The back view of the mounted device. (d)The top view of the mounted device.

After drilling the box, we could mount the PCB, the laser mount, switch and different ports on it. Put the laser diode into the socket of the laser mount, fix the photodiode on the PCB using screws and tape down the wiring of the fiber cable. Figure 4.6 shows the entire system and the mounted device from 3 views. The next step is to write an analog input program in LABVIEW to drive the NI USB-6211, which will be introduced in the next section.

Chapter 5

Calibration and Application Example

Before practical usage, the system should be calibrated. An application example of testing the Q factor of a microcavity is introduced in this section.

5.1 Calibration

For convenience of the practical usage, we should read the laser power directly on the monitor in LabVIEW by calculating the relationship between the analog signal voltage and the laser power received.

LabVIEW is short for Laboratory Virtual Instrument Engineering Workbench, which is a development environment for visual language "G-language" from National Instruments. LabVIEW is commonly used for data acquisition, instrument control, and industrial automation, and it could be installed in the major operating system including Windows, Unix and Linux.

Open the LabVIEW software, and connect the USB-6211's USB-port to PC, the driver will be installed automatically if the DAQmx driver is installed firstly and correctly. We could write an analog input program as Figure 5.1 shows if the USB-6211 is recognized. The DAQ Assistant module is set for the data capturing, and the export waveform module is used for recording the data.

Double click the DAQ Assistant, select the right channel connected to the photodiode and configure parameters as is shown in the Figure 5.2 shows. The Acquisition Mode should be set in continuous Samples, and the Max and Min voltages should be

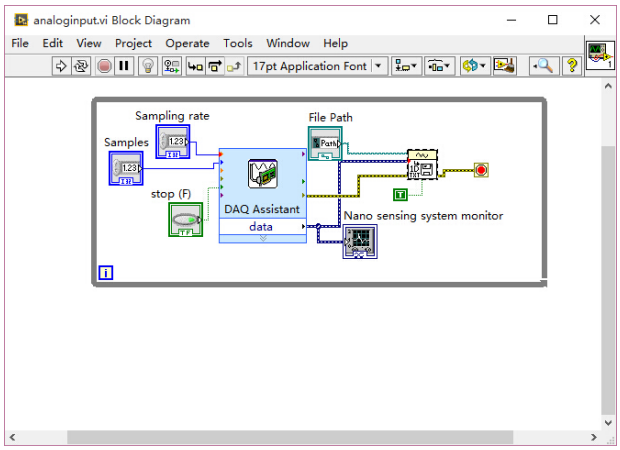

Figure 5.1: Analog input program in LabVIEW

set to 10 V and - 10V in case of a revise connection of the cable. The sampling rate and sample to read could be changed according to different accuracy requirement, for example, a sampling rate higher than 100k is usually used in the nano-sensing area.

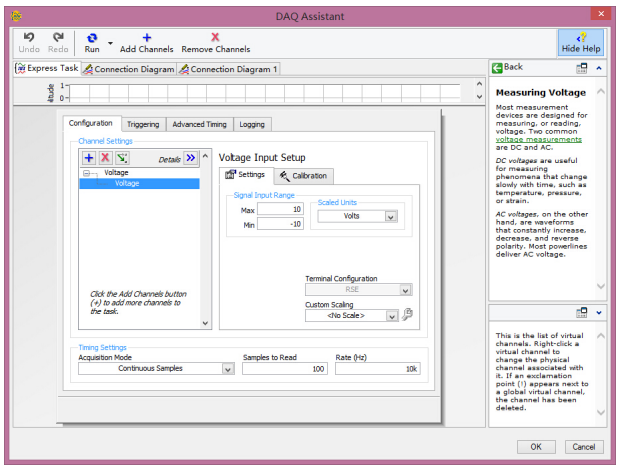

Figure 5.2: Analog input program parameters set in DAQ Assistant

Here we set the sample rate to 1 kHz and read 100 samples per loop. Figure 5.3 shows the front panel of the nano-sensing system after setting up, which will be discussed later.

After the whole system is set up, we should calibrate the laser diode and the photodiode and quantize the monitor graph to test other sensing beads.

Unmount the laser diode, and put the fiber into the socket of the optical spectrum analyzer, we get the related laser power distribution shown in Figure 5.4.

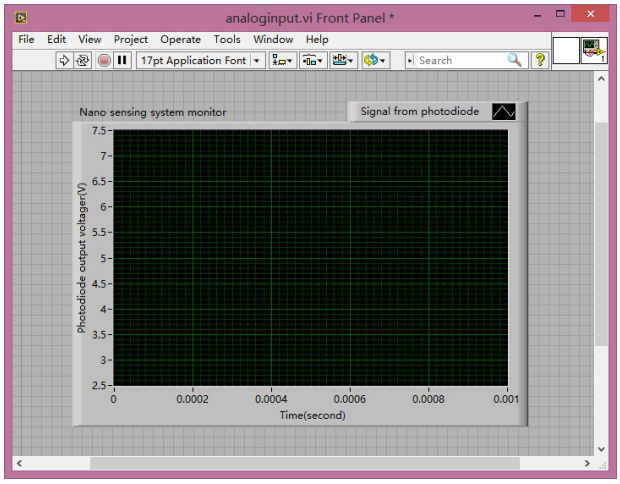

Figure 5.3: The front panel of analog input program after configuration

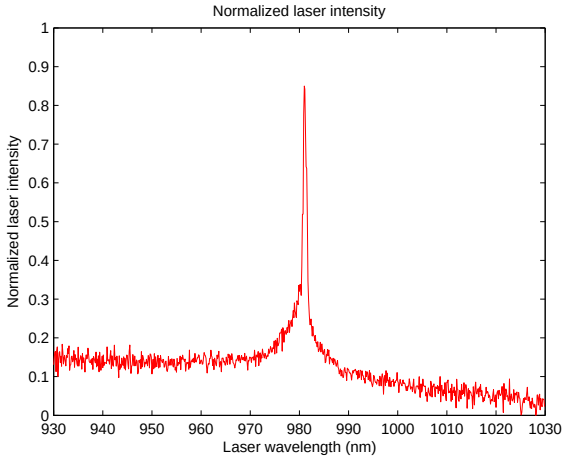

Figure 5.4: Normalized laser intensity on 100nm scales. The resolution bandwidth is 0.125 nm

As shown in Figure 5.4, the laser has a relative narrow and unique peak which is suitable for general usage.

By using the power meter, we could calibrate the output power and find its correlation with the output analog signal. Table 5.1 shows the relationship between the laser driver current, photodiode output voltage, and the related laser power.

TEC temperature: 24.99°C		
Laser driver current	analog output voltage	related laser power
15.03 mA	2.8 V	70.05μW
16.07 mA	3.0 V	0.45 mW
19.37 mA	3.5 V	1.66 mW
22.72 mA	4.0 V	2.84 mW
25.40 mA	4.5 V	3.77 mW
28.52 mA	5.0 V	4.83 mW
35.09 mA	6.0 V	7.08 mW
42.53 mA	6.8 V	10.12 mW

Table 5.1: Relationship between the laser driver current, photodiode output voltage, and the laser power.

The response output voltage of the photodiode is 2.8 to 6.8 V DC, where the minimum laser power is 70.05 μW and the maximum laser power is 10.12 mW. When the laser power is lower than the minimum or larger than the maximum value, the output voltage will stay at the related extremum. Figure 5.5 shows the relationship between the laser driver current and photodiode output voltage.

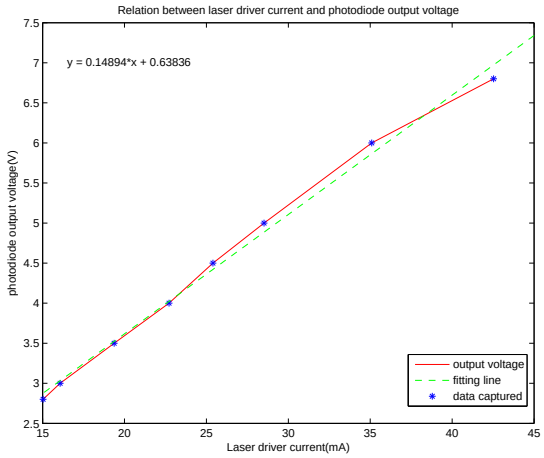

Figure 5.5: Relationship between the laser driver current and photodiode output voltage(TEC temperature: 24.99°C)

From Figure 5.5 we see the laser driver current and output voltage are linear. Figure 5.6 demonstrates that the photodiode output voltage is proportional to the laser

power, which means we can get the laser power easily from the related photodiode output voltage.

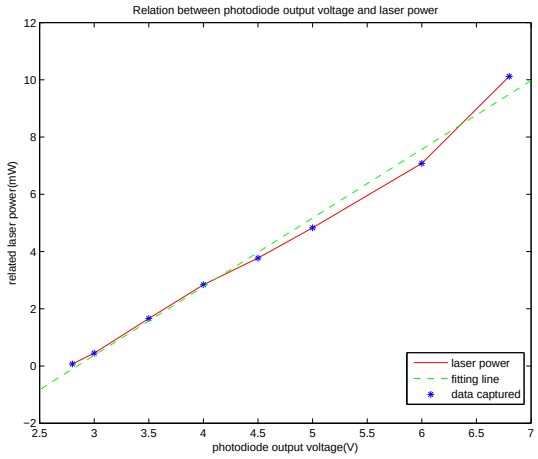

Figure 5.6: Relationship between the photodiode output voltage and the laser power(TEC temperature: 24.99°C).

According to Figure 5.6, we configure the front panel of the nano-sensing system monitor in LabVIEW as shown in Figure 5.7.

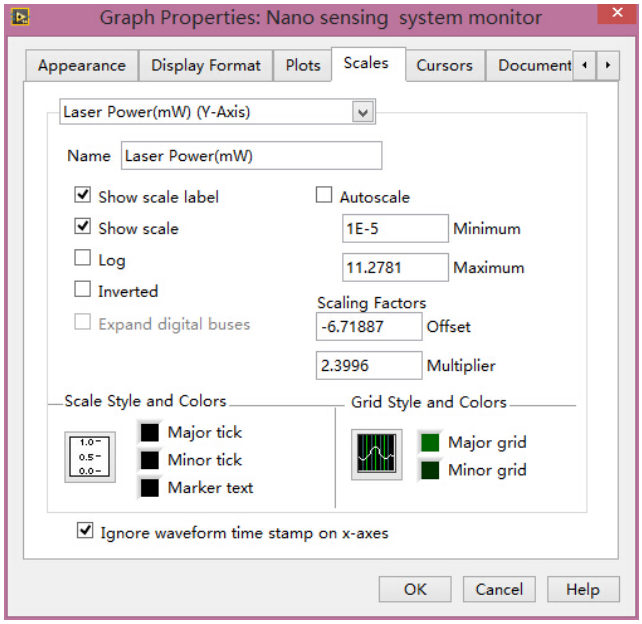

Figure 5.7: Configuration of the scales in the LabVIEW front panel.

First, right click the Y-axis of the coordinate system shown in Figure 5.3 and choose the property options. Under the **scales** menu, we could see the details of the

setting of the scales. Using the relationship in Figure 5.3, fill the two factors −6.8256 and 2.3996 into **Offset** and **Multiplier** blanks separately after we choose the Y-Axis from the list. Adjust the **Offset** to −6.71887 to move the origin near zero.

By applying settings mentioned above to the configuration, we could read laser power values directly in the front panel of the monitor shown in Figure 5.8.

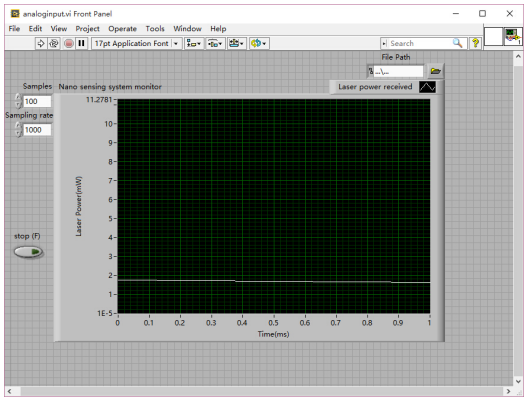

Figure 5.8: The front panel of the monitor in LabVIEW after calibration

A practical test for the working temperature and resolution of this system is introduced below.

Keep the laser driver current on 23.00 mA, adjust the TEC temperature from 0 to 50 °C,Figure 5.9 indicates the laser power captured under different temperature condition. The laser power in the figure is an average value calculated after the TEC temperature has stabilized.

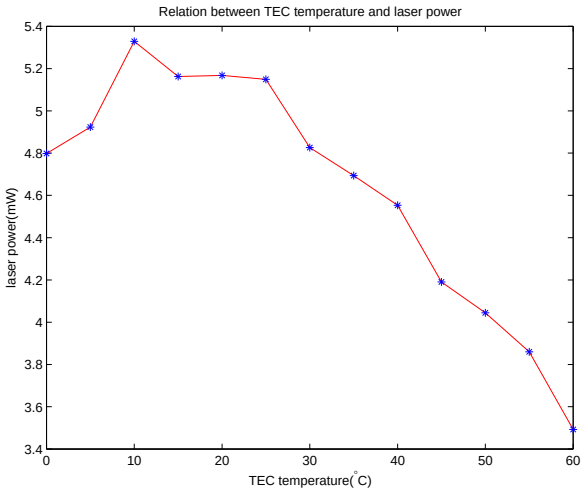

Figure 5.9: Relationship between TEC temperature and laser power

From the figure we observe that the laser power will decrease if the temperature is too low or too high. To achieve an ideal performance, the TEC temperature should be set between 10 and 25 °C.

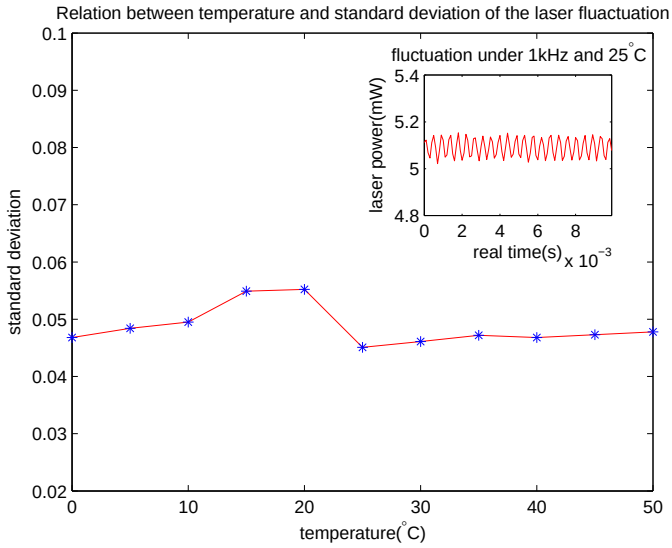

Figure 5.10: The standard deviations of laser fluctuation at different temperatures for a 1kHz sampling rate. The insert plot shows the laser fluctuation at 25 °C.

To determine the resolution of the system, we could keep all the environment variables unchanging to see the fluctuation of the laser power indicator. The differences of the data change should be larger than the standard deviation to be considered as variations. Figure 5.10 shows the standard deviations of the laser fluctuation these captured under 1kHz speed, 23.00 mA laser driver current in different temperatures. The average value of the standard deviations is 0.0486. That means the average resolution of this system is 0.05 mW under its working temperature ranges at 1k sampling rate. An unlocked laser diode, shifted fiber, and the performance of the photodiode all are the possible reasons limit the resolution of this system. In practical measurements, a high sampling rate is required to get a sensible result. Figure 5.11 shows the relationship between the sampling rate and the standard deviation of the laser fluctuation under 23.00 mA laser driver current and 25.00 °C TEC temperature. From the figure we can find that a high sampling rate improved a little bit of the resolution ability.

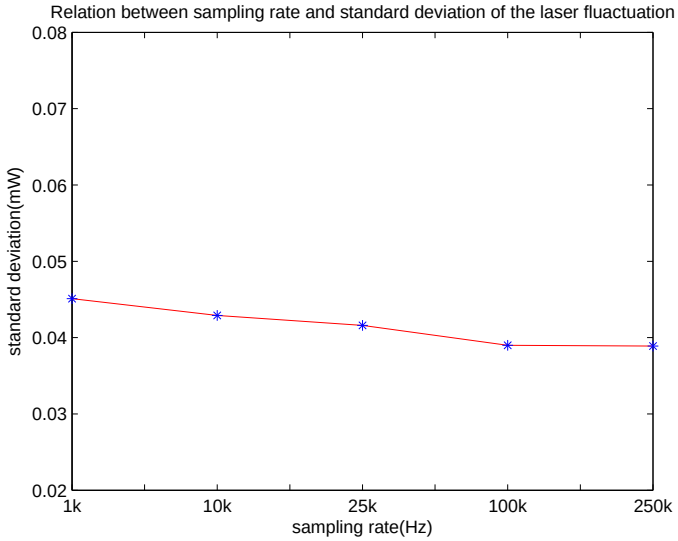

Figure 5.11: The standard deviations of laser fluctuation at different sampling rates under 25 °C condition.

5.2 Application example: Test the Q factor of a microcavity

After calibration, the device could be used in our experiment. For example, testing the Q factor of a microcavity, could be implemented by this system.

To use this sensing system, firstly we should connect all the devices together including the WGM resonator. Then plug in the power and turn on all the devices. To adjust the TEC temperature, we should press the **selection** button to turn green the **T** button in the **TEC DISPLAY** area. Make sure the **ON** button is green and press the **SET** button in the **TEC DISPLAY** button, and then rotate the knob to get the idea TEC temperature after press the **TEC** button under the adjust knob. The laser driver current tuning progress is similar to the adjustment of the TEC temperature. Before we turn on the laser, we should select the data store file in the dialog of LabVIEW.

The laser driver has a modulation function to modulate its driver current, and its interface is a BNC male port locates at the lower right-hand corner of the laser driver front panel. Connect the laser output with a tapered fiber, and then connect the optical loop back to the photodiode. According to the specification, the laser current has a modulation range from 0 to 10 V. Connect the function generator with a 10 dB attenuator to modulate the laser current. Set the TEC temperature at $25°C$, laser

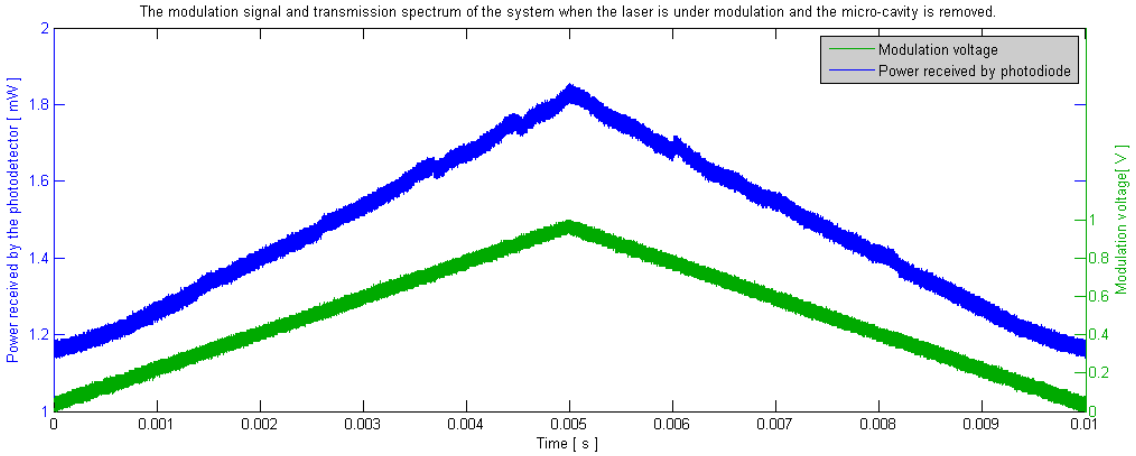

Figure 5.12: The modulation signal and transmission spectrum of the system when the laser is under modulation and no microcavity coupled.

current at 23.00 mA, and adjust the triangle modulation signal at 1 V amplitude, 500mV offset, 100 Hz scan rate.

The modulation of the laser driver can lead a slight change of the output laser center wavelength and its intensity at the same time. The change of the intensity by the modulation makes the transmission spectrum a triangle wave and it is shown on the blue line of the Figure 5.12. The modulation signal is shown in the green line in the Figure 5.12. The center wavelength of the laser is scanned in small range scale near 980nm at the same time.

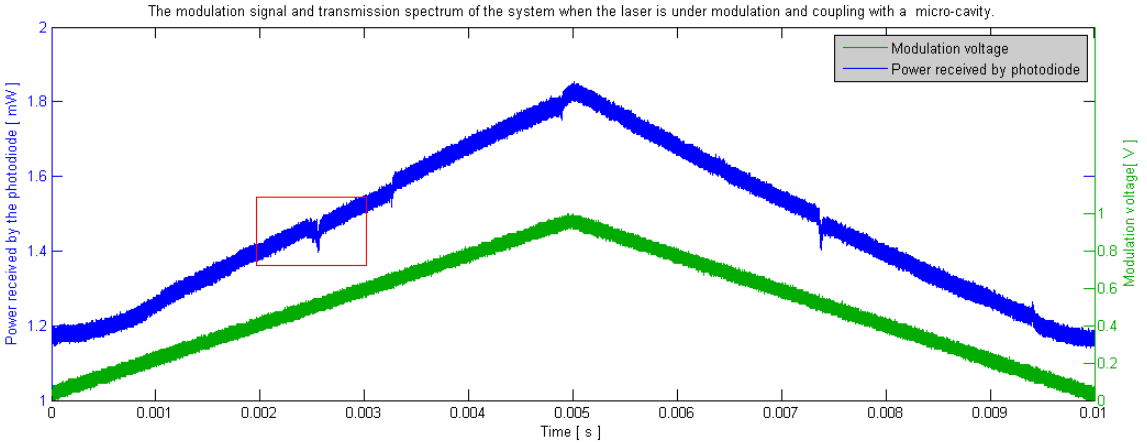

Figure 5.13: The modulation signal and transmission spectrum of the system when the laser is under modulation and coupling with a microcavity.

Keep the setup unchanging connect a microcavity coupled with the taped fiber,

Figure 5.13 shows the transmission spectrum when the system is coupling with a microcavity. The red box in the figure is a transmission dip and has been enlarged in Figure 5.14. To eliminate the effect of the intensity, we could subtract the trace from the Figure 5.13 from that of Figure 5.12. Figure 5.15 shows a result of the subtraction, and the zoom in view is also shown in Figure 5.16.

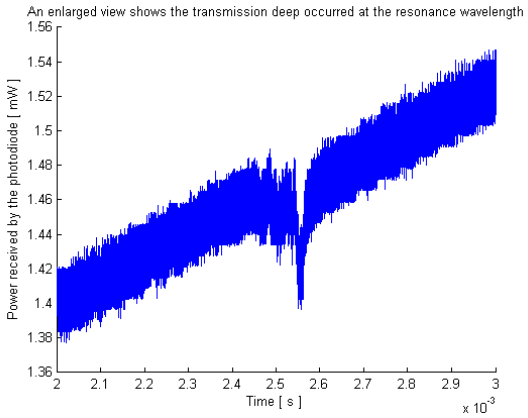

Figure 5.14: An enlarged view of the transmission dip occurred at the resonance wavelength of the microcavity.

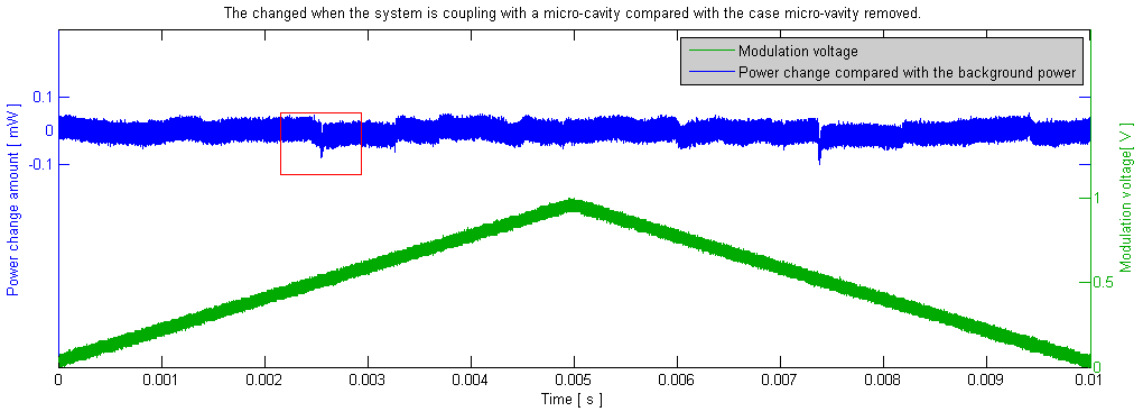

Figure 5.15: The power changed when the system is coupling with a microcavity compared with the case microcavity removed.

To calculate the Q factor of this dip, we should get the half width of the dip. One method is using the interferometer to see the proportion of the dip compared with the interferometer sinusoidal signal. But the laser diode is F-P type, which lead multiple modes lasing simultaneously plus the modulation of laser driver current lead the laser

intensity and center wavelength shifting at the same time, the interferometer signal becomes noisy and unrecognizable. Another method for calculating the Q factor is used here: we could measure the relationship between the modulation voltage, laser driver current, and the output intensity because of the intensity is also modulated by the laser driver current at the same time with the center wavelength.

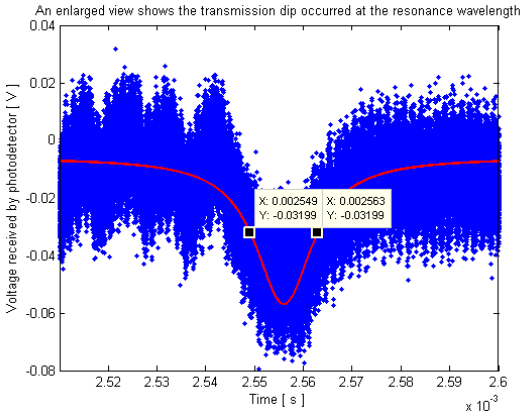

Figure 5.16: An enlarged view of the subtraction transmission dip occurred at the resonance wavelength of the microcavity.

Table 5.2 shows an experiment measurement of their values. Figure 5.17 shows the relationship between the laser driver current and the output power. We could see from the figure that the slope efficiency of this curve is 0.46 W/A, which close to a similar product with the laser diode. Its specification is shown in Table 5.3[1].

The modulation signal tunes the laser intensity and the laser center wavelength at the same time, which means they are proportional to each other on a small scale. According to the specification, the current tuning speed is approximately 0.002 nm/mA, to be more accurate, 0.0023 nm/mA. From the Figure 5.15, we could get the scan period is 0.01s (scan rate 100 Hz). The half period is 5×10^{-3} s. During this time, the signal modulates 1 voltage. And from the Figure 5.16 we could get the half wave width of the dip is 3.1×10^{-5} s. We could get the voltage tuning amount during this time, according to the proportion. The wavelength shift $\Delta\lambda$ is proportional to the shift of the laser driver, which is also proportional to the voltage tuning amount.

So we have:

$$\frac{T_{fullscan}}{T_{dip}} = \frac{\lambda_{fullscan}}{\Delta\lambda} \tag{5.1}$$

[1]https://www.thorlabs.com/thorcat/QTN/DBR976S-SpecSheet.pdf

The $\lambda_{fullscan}$ could be calculated according to the laser driver current tuning range and the slope efficiency.

modulation voltage(V)	laser driver current(mA)	output power(mW)
0.2	7.72	0.0018
0.4	15.47	0.187
0.6	23.22	4.07
0.8	30.96	7.91
1	38.7	11.78
1.2	46.44	15.57
1.4	54.18	19.36
1.6	61.92	22.68
1.8	69.66	26.11
2	77.39	29.43
2.2	85.12	33.22
2.4	92.85	36.98
2.6	100.42	42.13

Table 5.2: List of the relationship between the modulation voltage, laser driver current, and output power

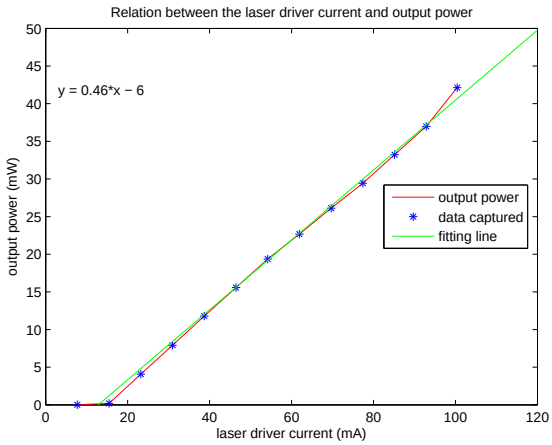

Figure 5.17: Relationship between the laser driver current and output power.

From Table 5.2, the laser current shift is 40 mA/V. The modulation signal is connected with a 10 dB attenuator. This means the modulation range is 100 mV,

and the laser driver current tuning range is 4 mA. So we could get the $\lambda_{fullscan}$ =0.0092 nm. Therefore, the $\Delta\lambda$ could be calculated, and its value is 5.5×10^{-5} nm.

According to:

$$Q = \frac{\lambda_r}{\Delta\lambda} \tag{5.2}$$

We could get the Q equals to 1.7×10^7.

DBR976S				
	Symbol	Min	Typical	Max
Center Wavelength	λ_c	971 nm	976 nm	981 nm
Laser linewidth	Δv	-	10 MHz	-
Output Power CW @I_{op}	P_{op}	35 mW	45 mW	-
Operating Current	I_{op}	-	150 mA	200mA
Mode Hop Rage	ΔI_{MH}	-	-	10mA
Mode Hop Free Rage	ΔI_{MHF}	60 mA	-	100mA
SMSR	SMSR	30dB	50dB	-
Threshold Current	I_{TH}	-	30 mA	-
Forward Voltage	V_F	-	2.0 V	2.5 V
Slope Efficiency	$\Delta P/\Delta$I	-	0.4 W/A	-
Current Tuning	$\Delta\lambda/\Delta I$	-	0.002 nm/mA	-
Temperature Tuning	$\Delta\lambda/\Delta T$	-	0.07 nm/$^\circ C$	-
Monitor Diode Responsivity	I_{MON}/P	-	10μA/mW	-

Table 5.3: Specifications for a similar laser diode with ADC 980S160GBAFC

A reference experiment using a laboratory New Focus TLB-6700 $Velocity^{TM}$ External Cavity Diode Laser with a 975 nm center wavelength is also implemented. Figure 5.18 shows the full-scan of the transmission spectrum, the modulation signal is set at 0 V offset, 500 mA amplitude, 100 Hz is used in this experiment. The up-scan is enlarged and shown in Figure 5.20.

The interferometer signal is a 21.3 MHz sinusoidal wave that could be used as a reference signal to measure the half width of the dip. From Figure 5.20, we calculate the half width of the dip Δf is 3.6 MHz. According to:

$$Q = \frac{f_r}{\Delta f} \tag{5.3}$$

The Q equals to 8.5×10^7.

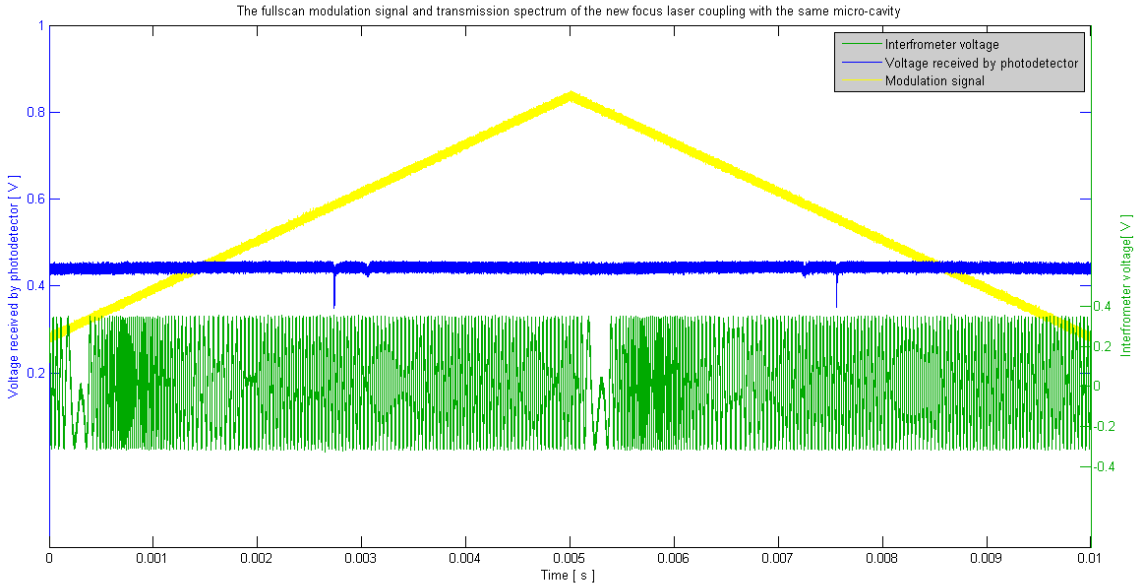

Figure 5.18: The full-scan modulation signal and transmission spectrum of the new focus laser coupling with the same microcavity.

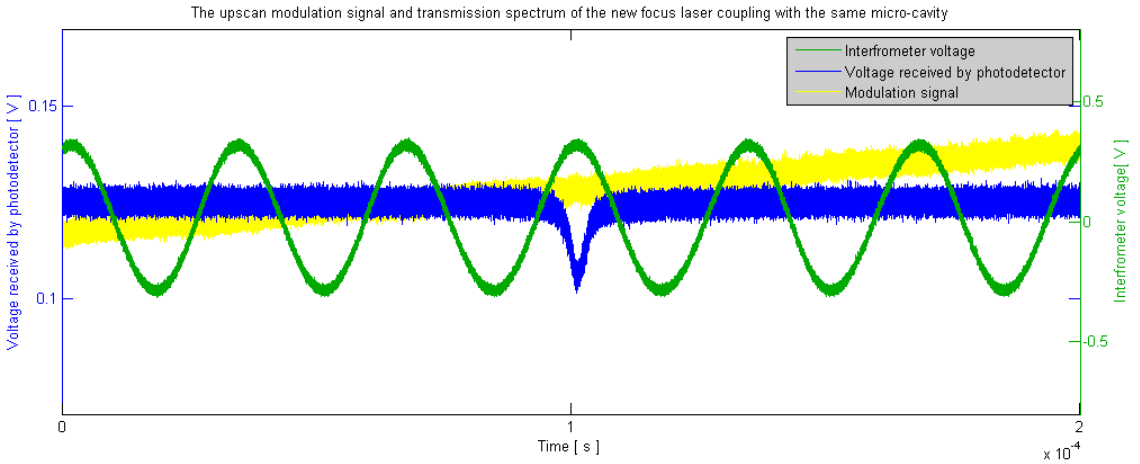

Figure 5.19: The up-scan modulation signal and transmission spectrum of the new focus laser coupling with the same microcavity.

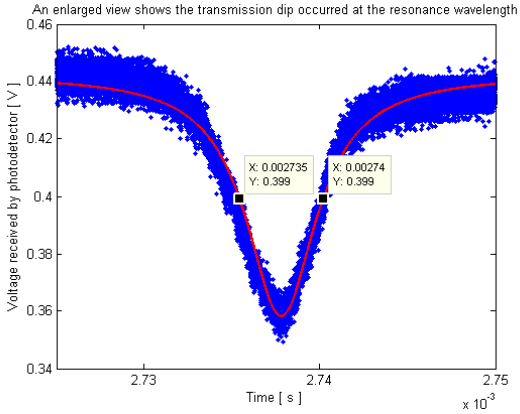

Figure 5.20: An enlarged view of the up-scan transmission spectrum dip of the new focus laser.

The differences of the New focus laser and the laser diode and used in the system is acceptable and it may due to the difference of their center wavelength and the insertion losses. Therefore, this system could be used to estimate and calculate the Q factor of a microcavity.

Chapter 6

Discussion

6.1 Summary

In summary, we built a nano-sensing system and assembled a laser diode and photodiode into a small device box working for the system. This device is small, movable and affordable for casual and wild usage after calibration. By using an ADC connected to a PC or laptop, we could read the laser power directly on our PC and laptop. The detachable socket allows us to change wavelength by swapping other laser diode and photodiode.

In this report, we introduced the selections of different modules for building the system economy and affordable. The system has a 980 nm central wavelength, 0.5 nm half peak width laser with a 160 mW maximum output power. The response range of the photodiode is up to 10 mW. A portable ADC, whose sampling rate could reach as high as 250 kHz, with associated program in LabVIEW is used to capture and record the data simply and easily. The resolution of the system is 0.05 mW and temperature response of the system is also tested from 0 to 50°C. All the parts are designed associated to make the device compact enough. To enhance the reliability and integrity, the laser diode module with the laser mount and the photodiode module are integrated into a device box. A power supply module with a switch is designed and assembled to meet the different requirements of the voltage level. The fibers are also tapered in this device to be protected from bending. At the last, An application example of testing the Q factor of microcavity is introduced.It proved the system can get a result which has a same order compared with a result of the New focus laser experiment.

6.2 Future work

This system is compact, affordable and approved could be used for testing Q factor of microcavity. However, It is still not a system with a high level of integration, which need an external laser driver and an AD converter connected. Besides, the output impedance of the photodiode is 50 Ω but the input impedance of the AD converter is larger than 10 $G\Omega$. A transimpedance amplifier should be applied for impedance matching in the future. Moreover, the resolution and accuracy level of the system could be improved. The next generation product could integrate a laser driving and an AD converter circuit into one small box. With a higher unimodality, immunity and stability of the laser diode and a wider response range of the photodiode, the system could be much more portable and sensitive in the future. A laser locking module is another way to improve the performance of the whole system.

Bibliography

[1] V. Sandoghdar, F. Treussart, J. Hare, V. Lefèvre-Seguin, J. M. Raimond, and S. Haroche, "Very low threshold whispering-gallery-mode microsphere laser," *Phys. Rev. A*, vol. 54, pp. R1777–R1780, Sep 1996. [Online]. Available: http://link.aps.org/doi/10.1103/PhysRevA.54.R1777

[2] J. W. S. L. Rayleigh), *The Theory of Sound*. New York: Dover, 1945.

[3] I. Teraoka, "Analysis of thermal stabilization of whispering gallery mode resonance," *Optics Communications*, vol. 310, pp. 212 – 216, 2014. [Online]. Available: http://www.sciencedirect.com/science/article/pii/S0030401813007402

[4] J. R. Buck and H. J. Kimble, "Optimal sizes of dielectric microspheres for cavity QED with strong coupling," *Phys. Rev. A: At., Mol., Opt. Phys.*, vol. 67, p. 033806, Mar 2003. [Online]. Available: http://link.aps.org/doi/10.1103/PhysRevA.67.033806

[5] S. M. Spillane, T. J. Kippenberg, and K. J. Vahala, "Ultralow-threshold raman laser using a spherical dielectric microcavity," *Nature*, vol. 415, no. 6872, pp. 621–623, Feb. 2002. [Online]. Available: http://dx.doi.org/10.1038/415621a

[6] G. Griffel, S. Arnold, D. Taskent, A. Serpengüzel, J. Connolly, and N. Morris, "Excitation of morphology dependent resonances of microspherical cavities using optical fibers," *Opt. Photon. News*, vol. 6, no. 12, pp. 21–22, Dec 1995. [Online]. Available: http://www.osa-opn.org/abstract.cfm?URI=opn-6-12-21

[7] T. Lu, H. Lee, T. Chen, S. Herchak, J.-H. Kim, S. E. Fraser, R. C. Flagan, and K. Vahala, "High sensitivity nanoparticle detection using optical microcavities," *Proc. Natl. Acad. Sci. U. S. A.*, 2011. [Online]. Available: http://www.pnas.org/content/early/2011/03/21/1017962108.abstract

[8] B. Little, S. Chu, P. Absil, J. Hryniewicz, F. Johnson, F. Seiferth, D. Gill, V. Van, O. King, and M. Trakalo, "Very high-order microring resonator filters for wdm applications," *Photonics Technology Letters, IEEE*, vol. 16, no. 10, pp. 2263–2265, Oct 2004.

[9] N. Nguyen, N. Gupta, T. Ioppolo, and M. ?tgen, "Whispering gallery mode-based micro-optical sensors for structural health monitoring of composite materials," *Journal of Materials Science*, vol. 44, no. 6, pp. 1560–1571, 2009. [Online]. Available: http://dx.doi.org/10.1007/s10853-008-3163-3

[10] T. Ioppolo, "Whispering gallery mode-based micro optical sensors for aerospace applications," p. 149, 2008, copyright ProQuest, UMI Dissertations Publishing 2008; updated on 2014-01-22;. [Online]. Available: http://search.proquest.com.ezproxy.library.uvic.ca/docview/193716578?accountid=14846

[11] S. Berneschi, F. Baldini, F. Cosi, M. Ferrari, G. N. Conti, S. Pelli, S. Soria, and G. C. Righini, "Optical microspherical resonators for biomedical applications," in *Frontiers in Optics 2010/Laser Science XXVI*. Optical Society of America, 2010, p. FWF5. [Online]. Available: http://www.osapublishing.org/abstract.cfm?URI=FiO-2010-FWF5

[12] A. Oraevsky, "Whispering-gallery waves," vol. 32, pp. 377C–400, 2002.

[13] J. E. V. L. G. L. C. M. V. M. M. Bass, C. DeCusatis and E. V. Stryland, *Handbook of Optics, Third Edition Volume IV: Optical Properties of Materials, Nonlinear Optics, Quantum Optics (set), ser. Handbook of Optics.* Mcgraw-hill, 2009.

[14] A. Byrnes, R. Pant, E. Li, D.-Y. Choi, C. G. Poulton, S. Fan, S. Madden, B. Luther-Davies, and B. J. Eggleton, "Photonic chip based tunable and reconfigurable narrowband microwave photonic filter using stimulated brillouin scattering," *Opt. Express*, vol. 20, no. 17, pp. 18 836–18 845, Aug 2012. [Online]. Available: http://www.opticsexpress.org/abstract.cfm?URI=oe-20-17-18836

[15] E. Hamidi, D. Leaird, and A. Weiner, "Tunable programmable microwave photonic filters based on an optical frequency comb," *Microwave Theory and Techniques, IEEE Transactions on*, vol. 58, no. 11, pp. 3269–3278, Nov 2010.

[16] P. Rabiei, W. H. Steier, C. Zhang, and L. R. Dalton, "Polymer micro-ring filters and modulators," *J. Lightwave Technol.*, vol. 20, no. 11, p. 1968, Nov 2002. [Online]. Available: http://jlt.osa.org/abstract.cfm?URI=jlt-20-11-1968

[17] S.-J. Choi, W. Lin, K. Djordjev, S. Choi, P. D. Dapkus, G. Griffel, R. Menna, and J. Connolly, "Microring resonators vertically coupled to buried heterostructure bus waveguides," in *Integrated Photonics Research*. Optical Society of America, 2003, p. ITuE2. [Online]. Available: http://www.osapublishing.org/abstract.cfm?URI=IPR-2003-ITuE2

[18] D. Rabus, M. Hamacher, U. Troppenz, and H. Heidrich, "High-q channel-dropping filters using ring resonators with integrated soas," *Photonics Technology Letters, IEEE*, vol. 14, no. 10, pp. 1442–1444, Oct 2002.

[19] M. Lohmeyer, "Mode expansion modeling of rectangular integrated optical microresonators," *Optical and Quantum Electronics*, vol. 34, no. 5-6, pp. 541–557, 2002. [Online]. Available: http://dx.doi.org/10.1007/BF02892616

[20] A. L. Huston and J. D. Eversole, "Strain-sensitive elastic scattering from cylinders," *Opt. Lett.*, vol. 18, no. 13, pp. 1104–1106, Jul 1993. [Online]. Available: http://ol.osa.org/abstract.cfm?URI=ol-18-13-1104

[21] V. Ilchenko, P. Volikov, V. Velichansky, F. Treussart, V. Lefvre-Seguin, J.-M. Raimond, and S. Haroche, "Strain-tunable high-q optical microsphere resonator," *Optics Communications*, vol. 145, no. 1C6, pp. 86 – 90, 1998. [Online]. Available: http://www.sciencedirect.com/science/article/pii/S0030401897004392

[22] H. Tapalian, J.-P. Laine, and P. Lane, "Thermooptical switches using coated microsphere resonators," *Photonics Technology Letters, IEEE*, vol. 14, no. 8, pp. 1118–1120, Aug 2002.

[23] O. Schwelb, , and n Frigyes, "All-optical tunable filters built with discontinuity-assisted ring resonators," *J. Lightwave Technol.*, vol. 19, no. 3, p. 380, Mar 2001. [Online]. Available: http://jlt.osa.org/abstract.cfm?URI=jlt-19-3-380

[24] S. Chu, W. Pan, S. Sato, T. Kaneko, B. Little, and Y. Kokubun, "Wavelength trimming of a microring resonator filter by means of a uv sensitive polymer

overlay," *Photonics Technology Letters, IEEE*, vol. 11, no. 6, pp. 688–690, June 1999.

[25] J. K. S. Poon, Y. Huang, G. T. Paloczi, A. Yariv, C. Zhang, and L. R. Dalton, "Wide-range tuning of polymer microring resonators by the photobleaching of cld-1 chromophores," *Opt. Lett.*, vol. 29, no. 22, pp. 2584–2586, Nov 2004. [Online]. Available: http://ol.osa.org/abstract.cfm?URI=ol-29-22-2584

[26] A. A. Savchenkov, V. S. Ilchenko, T. Handley, and L. Maleki, "Ultraviolet-assisted frequency trimming of optical microsphere resonators," *Opt. Lett.*, vol. 28, no. 8, pp. 649–650, Apr 2003. [Online]. Available: http://ol.osa.org/abstract.cfm?URI=ol-28-8-649

[27] A. Savchenkov, V. Ilchenko, T. Handley, and L. Maleki, "Second-order filter response with series-coupled silica microresonators," *Photonics Technology Letters, IEEE*, vol. 15, no. 4, pp. 543–544, April 2003.

[28] A. Savchenkov, V. Ilchenko, A. Matsko, and L. Maleki, "Tunable filter based on whispering gallery modes," *Electronics Letters*, vol. 39, no. 4, pp. 389–391, Feb 2003.

[29] V. S. Ilchenko, A. A. Savchenkov, A. B. Matsko, and L. Maleki, "Nonlinear optics and crystalline whispering gallery mode cavities," *Phys. Rev. Lett.*, vol. 92, p. 043903, Jan 2004. [Online]. Available: http://link.aps.org/doi/10.1103/PhysRevLett.92.043903

[30] P. Urquhart, "Compound optical-fiber-based resonators," *J. Opt. Soc. Am. A*, vol. 5, no. 6, pp. 803–812, Jun 1988. [Online]. Available: http://josaa.osa.org/abstract.cfm?URI=josaa-5-6-803

[31] K. Oda, N. Takato, and H. Toba, "A wide-fsr waveguide double-ring resonator for optical fdm transmission systems," *Lightwave Technology, Journal of*, vol. 9, no. 6, pp. 728–736, Jun 1991.

[32] B. Little, S. Chu, H. Haus, J. Foresi, and J.-P. Laine, "Microring resonator channel dropping filters," *Lightwave Technology, Journal of*, vol. 15, no. 6, pp. 998–1005, Jun 1997.

[33] J. Hryniewicz, P. Absil, B. Little, R. Wilson, and P.-T. Ho, "Higher order filter response in coupled microring resonators," *Photonics Technology Letters, IEEE*, vol. 12, no. 3, pp. 320–322, March 2000.

[34] C. G. B. Garrett, W. Kaiser, and W. L. Bond, "Stimulated emission into optical whispering modes of spheres," *Phys. Rev.*, vol. 124, pp. 1807–1809, Dec 1961. [Online]. Available: http://link.aps.org/doi/10.1103/PhysRev.124.1807

[35] P. Walsh and G. Kemeny, "Laser operation without spikes in a ruby ring," *Journal of Applied Physics*, vol. 34, no. 4, 1963.

[36] H.-M. Tzeng, K. F. Wall, M. B. Long, and R. K. Chang, "Laser emission from individual droplets at wavelengths corresponding to morphology-dependent resonances," *Opt. Lett.*, vol. 9, no. 11, pp. 499–501, Nov 1984. [Online]. Available: http://ol.osa.org/abstract.cfm?URI=ol-9-11-499

[37] W. Liang, V. S. Ilchenko, A. A. Savchenkov, A. B. Matsko, D. Seidel, and L. Maleki, "Whispering-gallery-mode-resonator-based ultranarrow linewidth external-cavity semiconductor laser," *Opt. Lett.*, vol. 35, no. 16, pp. 2822–2824, Aug 2010. [Online]. Available: http://ol.osa.org/abstract.cfm?URI=ol-35-16-2822

[38] I. S. Grudinin and L. Maleki, "Ultralow-threshold raman lasing with caf2 resonators," *Opt. Lett.*, vol. 32, no. 2, pp. 166–168, Jan 2007. [Online]. Available: http://ol.osa.org/abstract.cfm?URI=ol-32-2-166

[39] J.-Z. Zhang and R. K. Chang, "Generation and suppression of stimulated brillouin scattering in single liquid droplets," *J. Opt. Soc. Am. B*, vol. 6, no. 2, pp. 151–153, Feb 1989. [Online]. Available: http://josab.osa.org/abstract.cfm?URI=josab-6-2-151

[40] J.-Z. Zhang, G. Chen, and R. K. Chang, "Pumping of stimulated raman scattering by stimulated brillouin scattering within a single liquid droplet: input laser linewidth effects," *J. Opt. Soc. Am. B*, vol. 7, no. 1, pp. 108–115, Jan 1990. [Online]. Available: http://josab.osa.org/abstract.cfm?URI=josab-7-1-108

[41] J. Zhu, Ş. K. Özdemir, H. Yilmaz, B. Peng, M. Dong, M. Tomes, T. Carmon, and L. Yang, "Interfacing whispering-gallery microresonators and free space light

with cavity enhanced Rayleigh scattering," *Scientific Reports*, vol. 4, p. 6396, Sep. 2014.

[42] V. Braginsky, M. Gorodetsky, and V. Ilchenko, "Quality-factor and nonlinear properties of optical whispering-gallery modes," *Physics Letters A*, vol. 137, no. 7, pp. 393 – 397, 1989. [Online]. Available: http://www.sciencedirect.com/science/article/pii/0375960189909122

[43] M. O. Scully and P. A. Lee, "Frequency-pulling effects in josephson radiation," *Phys. Rev. Lett.*, vol. 22, pp. 23–26, Jan 1969. [Online]. Available: http://link.aps.org/doi/10.1103/PhysRevLett.22.23